Hersh Acoustical Engineering, Inc.

22305 Cairnloch Street
Calabasas, California 91302
818/224-4699   Fax: 818/224-4639
haeash@charter.net

Contract NNX09CF01

A2.03-9848. Numerical and Physical Modeling of the Response of Resonator Liners to Intense Sound and Grazing Flow

Final Report

Prepared by

Alan S. Hersh, Ph.D.

Vice President

and

Dr. Christopher Tam

Robert O. Lawton Distinguished Professor of FSU

Department of Mathematics

July 11, 2009

Submitted to:
COTR
Michael G. Jones'
NASA Langley Research Center

1. INTRODUCTION

The report is divided into two principal parts, the first consisting of the application of direct numerical simulation (DNS) to the study of the impedance of slit resonators constructed with slit orifices at high temperature and the computational investigation of their acoustic performance exposed to discrete and broadband sound.

The second consists of the development of a uniform grazing flow 1-dof impedance model of series coupled Helmholtz resonators constructed with multi-circular orifices and the development of a non-grazing flow, high amplitude, 2-dof impedance model of resonators constructed with multi-slit orifices.

2. COMPUTATIONAL INVESTIGATION OF THE EFFECT OF HiGH TEMPERATURE ON RESONATOR IMPEDANCE

In our computational study of resonator impedance, the impedance of a resonator at standard temperature (15^0 C) and a temperature representative of that of the primary jet of commercial jet engines (600^0 K) were investigated. For this study, the resonators were mounted at the end of a normal incidence impedance tube as shown in Fig. 2.1 and Fig. 2.2.
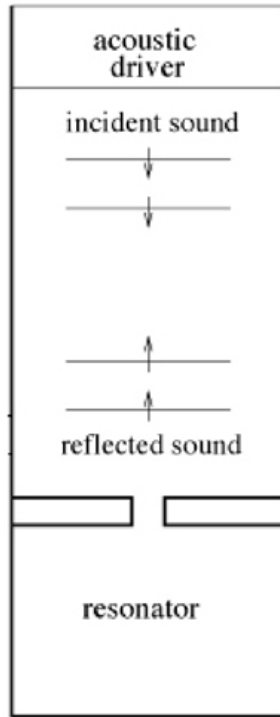

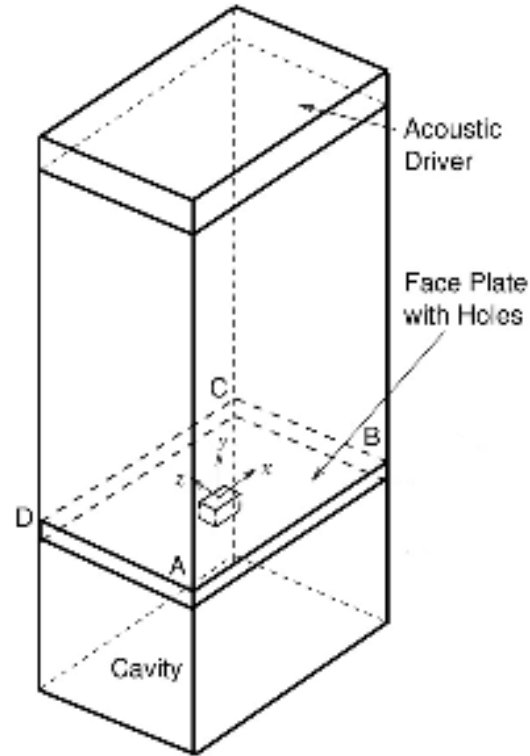| Figure 2.1. A slit resonator	Figure 2.2. A resonator with a rectangular
in an impedance tube.	opening in an impedance tube.

Fig. 2.1 shows a slit resonator. Fig. 2.2 shows a resonator with a rectangular opening in a normal incidence impedance tube. In our investigation, both discrete frequency and broadband incident sound are used in the simulation.

A significant rise in gas temperature would affect many of the properties of a gas, e. g. density, ratio of specific heats, speed of sound and viscosity. It is not straightforward to see how it might impact on the impedance of a liner. To characterize temperature effect, it is necessary to decide on a basis for comparison. For this purpose, it will be assumed that the source of sound is from another part of the system unaffected by the temperature change. In other words, the sound intensity and frequencies are the same. However, because the speed of sound increases with temperature, the depth mode resonance frequency of a resonator will increase. Thus to evaluate high temperature effect, the resonator depth has to be increased to keep the resonance frequency of the resonator the same. Figures 2.3 and Fig. 2.4 show the geometry of a slit resonator with the same resonance frequency used in the present study. One operates at 15^0 C and the other at 600^0 K.
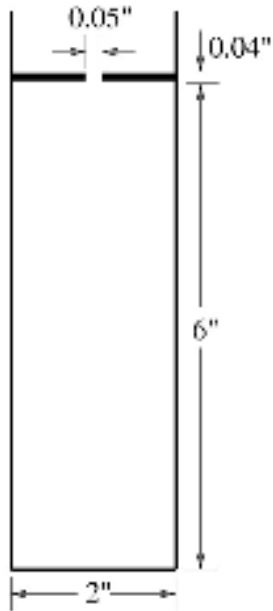
Fig. 2.3. 15^0 C resonator.   Fig. 2.4. 600^0 K resonator.

Incident Sound at Discrete Frequency

A series of numerical simulations at an incident sound wave frequency of 2 kHz were carried out. The incident sound-pressure-level (SPL) ranges from 115 dB to 145 dB. This spans the low SPL range, when the liner dissipation is through viscous damping at the resonator opening, to the high SPL range, when vortex shedding is the dominant dissipation mechanism. Figure 2.5 shows the measured resistance from the simulation data. Figure 2.6 shows the measured reactance. The results are presented in a normalized form (scaled to the value of ρa at the operating temperature) and in absolute level in Rayl.
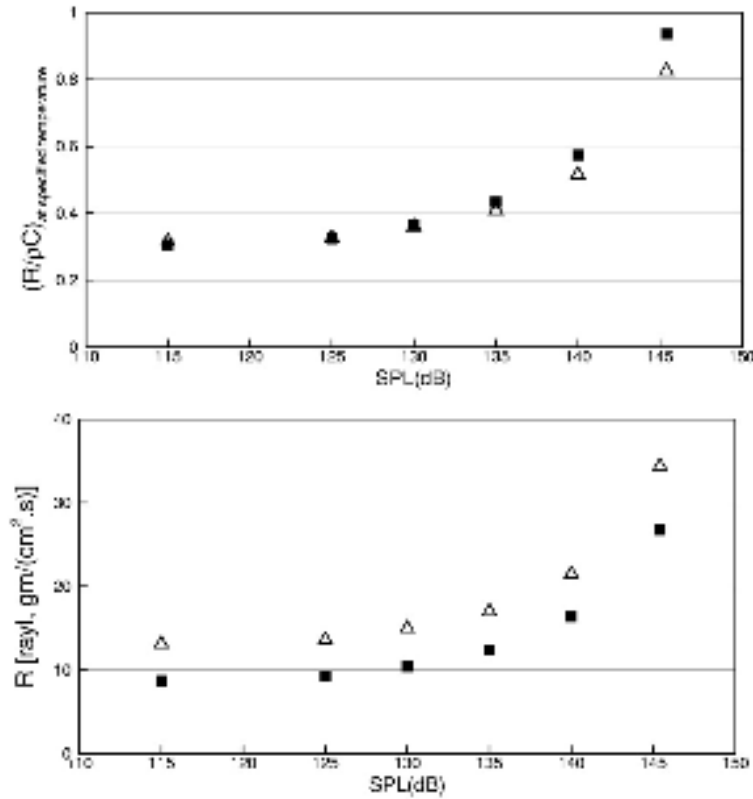
Figure 2.5. Resistance at 2 kHz. ■ 600^0 K; △ 15^0 C.

Figure 2.7. shows the corresponding absorption coefficient. At a fixed frequency, the resistance remains unchanged at low SPL. Around SPL = 130 dB, the resistance starts to increase with SPL. This marks the beginning of the nonlinear behavior of the resonator impedance. As SPL continues to increase, vortex shedding begins. This is accompanied by a steeper increase in resistance. On the other hand, the reactance tends to remain relatively constant. A small decrease occurs at even higher SPL. This behavior applies to resonator at low as well as at high temperature. The absorption coefficient generally follows the trend of the resistance.

On comparing the resistance and reactance at 15^0 C and at 600^0 K, it is clear that there are large differences when expressed in Rayl. In other words, temperature has a significant impact on the absolute value of the impedance of a resonator. However, when expressed in normalized form, the differences are much smaller. Since the normalized impedance is more relevant to the performance of a resonator, temperature effect is not exceedingly large. A better gauge of temperature effect, perhaps, is to use the absorption coefficient which is non-dimensional and is, therefore, independent of normalization.
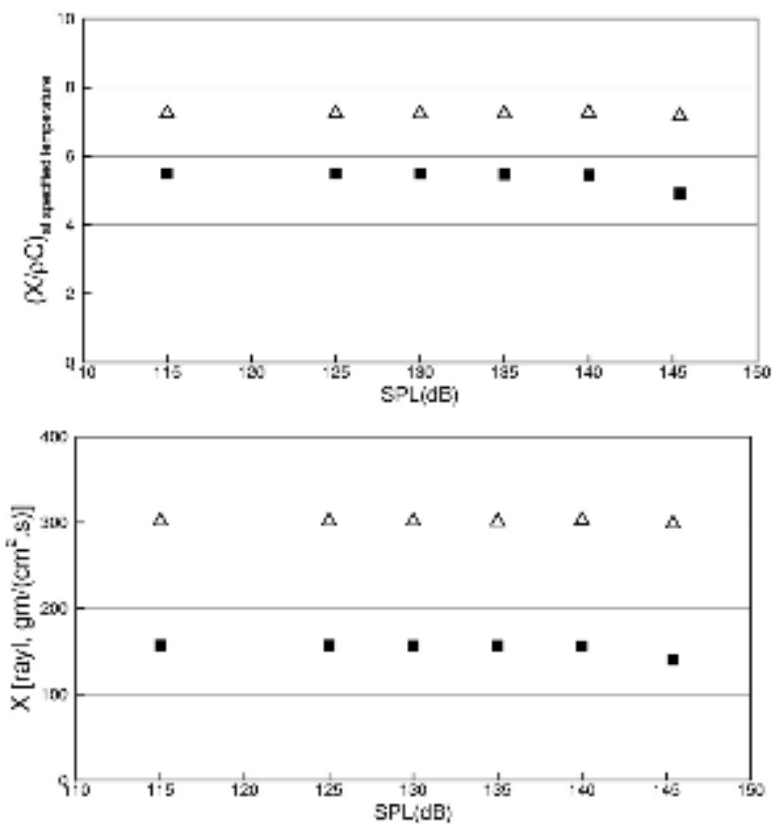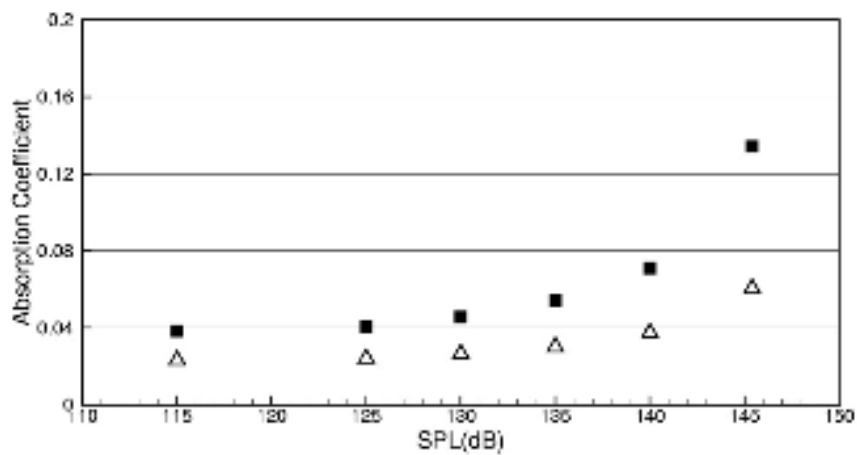
4

Figure 2.6. Reactance at 2 kHz. ■ 600^0 K; △ 15^0 C.

Figure 2.7. Absorption Coefficient at 2 kHz. ■ 600^0 K; △ 15^0 C.

Incident Sound at Quarter-Wave Resonance Frequency

A resonator would respond with large amplitude acoustic oscillations when excited at quarter-wave resonance frequency. It is, therefore, interesting to observe the effect of temperature on the resonator impedance at such resonance frequencies. In the present study, the test frequencies are chosen to be at 0.5, 1.0, 1.5, 2.0, 2.5 and 3.0 kHz. At each selected frequency, the depth of the resonator is adjusted to be exactly at ¼ wave length deep for the particular operating temperature. The measured resistance, reactance and absorption coefficients are shown in Figures 8, 9 and 10. The incident sound SPL at 0.5, 1.0, 1.5, 2.0, 2.5 and 3.0 kHz are respectively 151.6, 152.8, 151.9, 145.4 142.6 and 141.6 dB.
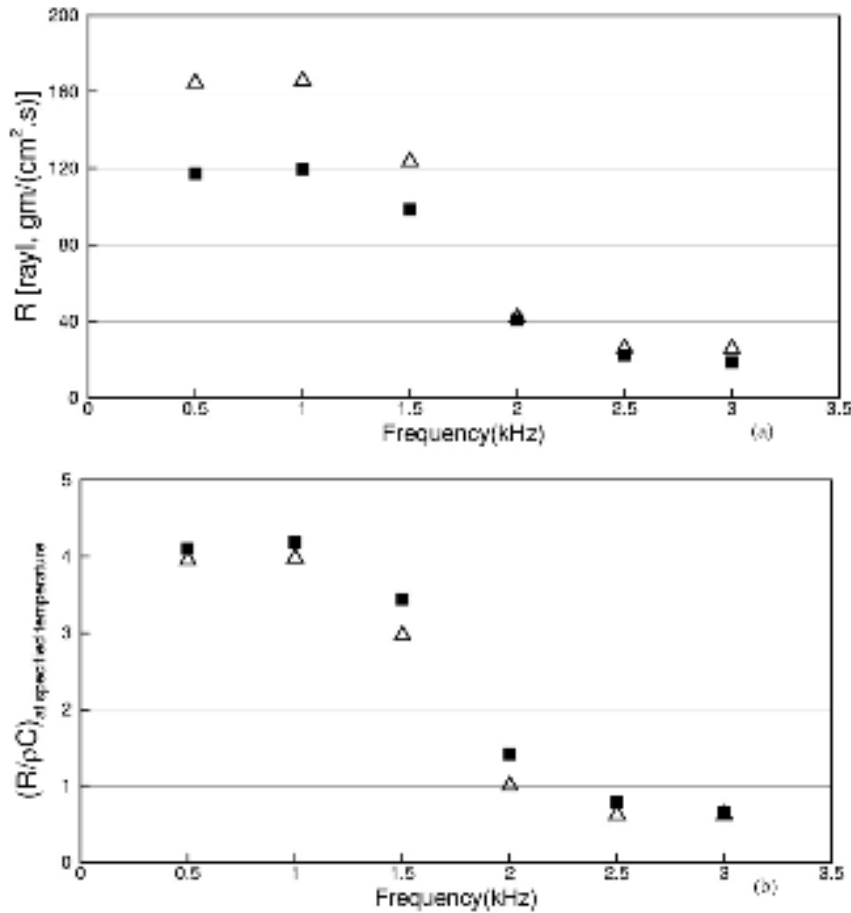

Figure 2.8. Resistance, normalized and in absolute unit, at quarter-wave resonance.

■ 600^0 K; △ 15^0 C.

For the resistance in normalized form, the effect of temperature is minimal. The absolute values are, however, quite different at low frequencies. The effect of temperature on reactance at quarter-wave resonances is quite different. It is higher at low temperature, regardless whether it is in normalized or in absolute value. The difference increases with frequency. The absorption coefficient, as in the non-resonance cases, is nearly independent of temperature.
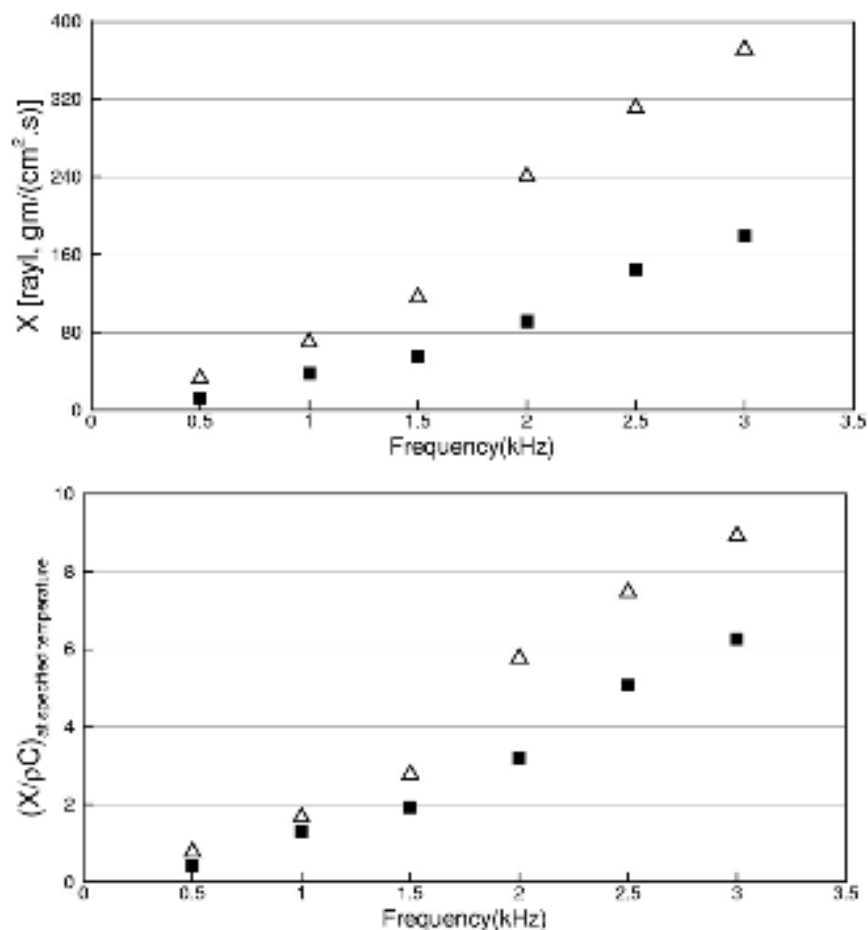

Figure 2.9. Reactance, normalized and in absolute unit, at quarter-wave resonance.
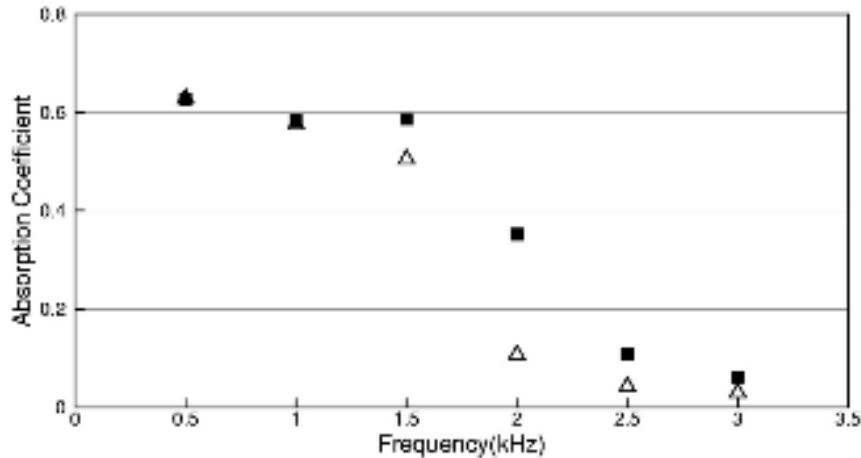
■ 600⁰ K; △ 15⁰ C.

Figure 2.10. Absorption coefficients at quarter-wave resonance.

■ 600^0 K; △ 15^0 C.

Broadband Incident Sound

The acoustic behavior of a resonator under broadband sound excitation is usually different from that under discrete incident sound waves. We performed a series of 3 dimensional simulations with broadband incident sound. The simulations use the same normal incidence impedance tube as in AIAA Paper 2009-3171. The impedance tube at 15^0 C is shown in Fig. 2.11. The depth of the resonator at 600^0 K is adjusted so as to have the same depth mode resonance frequency. The size of the rectangular opening is 0.05" by 0.0625". That is, the aspect ratio is 1.25.

Two direct numerical simulations have been carried out. One has an incident OASPL = 141 dB, the other has an OASPL of 150 dB. The incident sound spectra are shown in Fig. 2.12 and Fig. 2.17. They are the same as those in AIAA Paper 2009-3171. Fig. 2.12 shows the incident broadband noise spectrum at 141 OASPL (dotted line) measured experimentally. The spectrum covers the range of 500 Hz to 3000 Hz. In the numerical simulation, the spectrum is divided into 118 bands. The circles in Fig. 2.12 are the center frequencies of the bands. As can be seen the discretized spectrum (full line) is a very close approximation of that of the experiment.
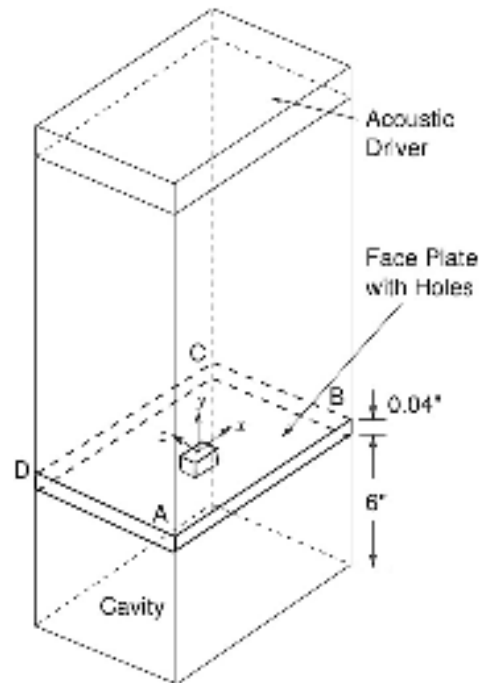
Figure 2.11. Normal incidence impedance tube used for numerical simulation with broadband incident sound waves.

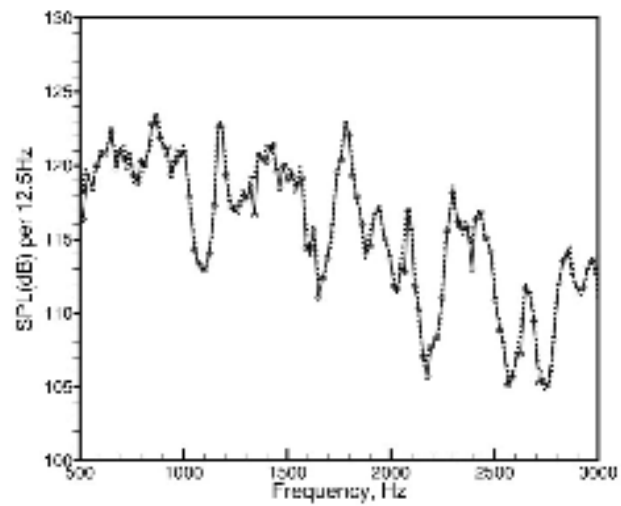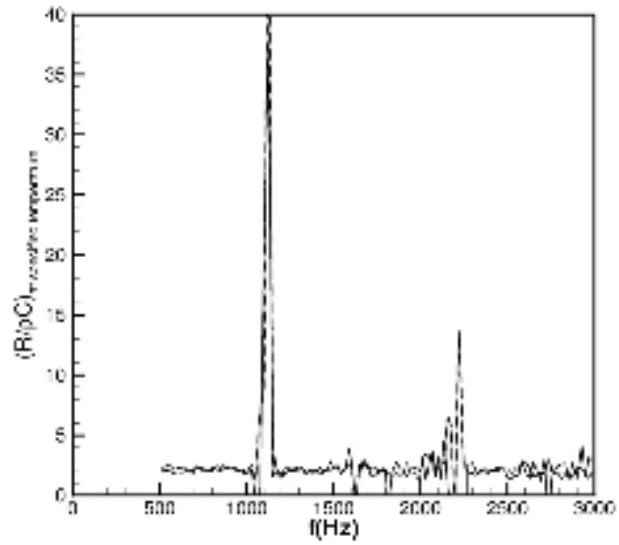Figure 2.12. Incident sound spectrum with an OASPL of 141 dB.

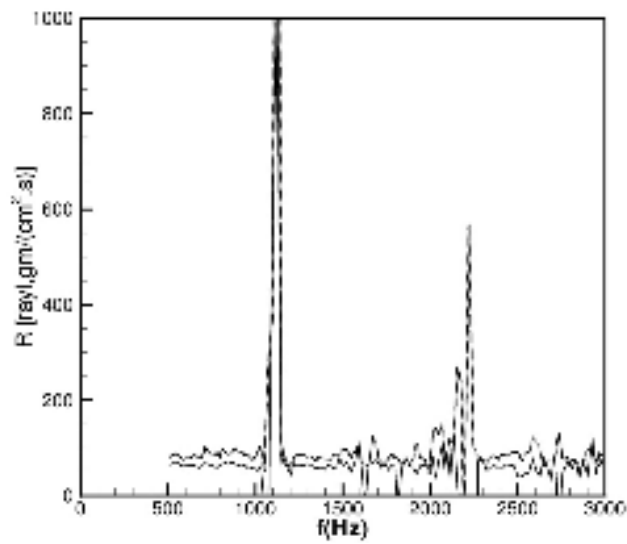Fig. 2.13. Resistance in normalized form. Solid line 600^0 K, dotted line 15^0 C. SPL=141 dB.

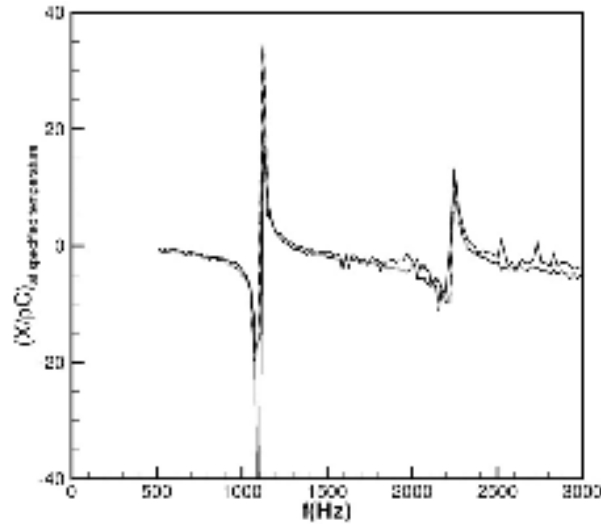Figure 2.14. Resistance in Rayl. Solid line 600^0 K, dotted line 15^0 C. SPL=141 dB.

Figure 2.15. Reactance in normalized form. Solid line 600^0 K, dotted line 15^0 C. SPL=141 dB.
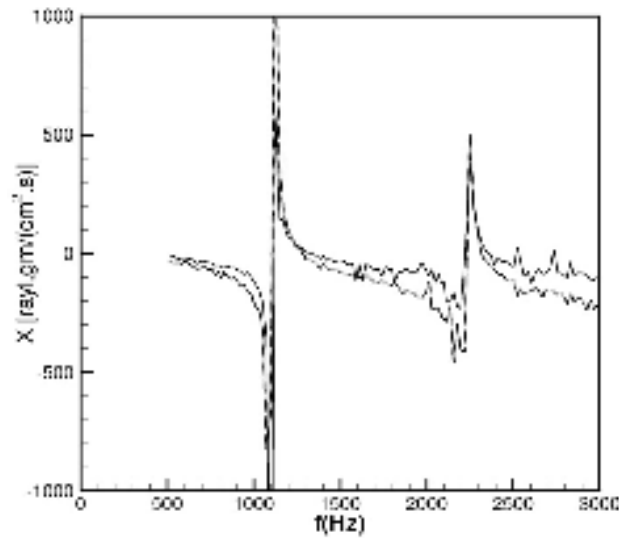
Figure 2.16. Reactance in Rayl. Solid line 600^0 K, dotted line 15^0 C. SPL=141 dB.

The above figures are the computed results at OASPL 140 dB. Collectively, they show that in the normalized form the impedance of a resonator is almost independent of temperature. When plotted in absolute unit, the impedance at 15^0 C is consistently higher (more negative if X is negative). The absorption coefficient, on the other hand, behaves somewhat differently. It is independent of temperature at low frequency. But at high frequencies there is more absorption at low temperature.
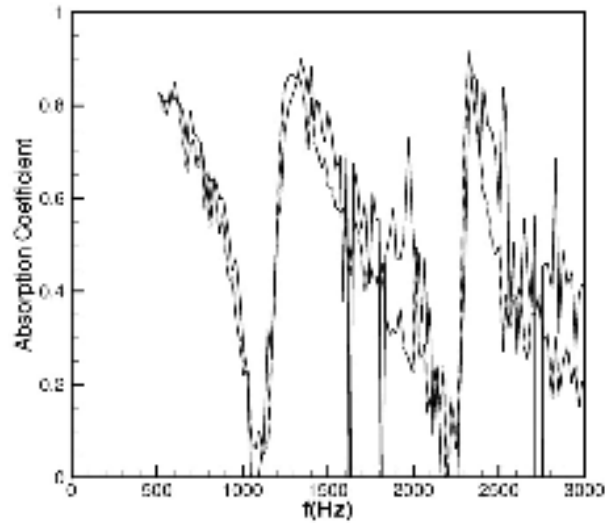
Figure 2.17. Absorption Coefficient. Solid line 600^0 K, dotted line 15^0 C. SPL=141 dB.

Figures 2.18 to 2.22 show similar results but at a much higher level of incident OASPL i.e. 150 dB. The trend involving temperature is, however, nearly the same as that at lower incident SPL. This indicates that the general trend is pretty much SPL independent. Since at 141 dB the resonator behaves linearly while at 150 dB the resonator behaves nonlinearly, the trend is most probably true for all levels of SPL.
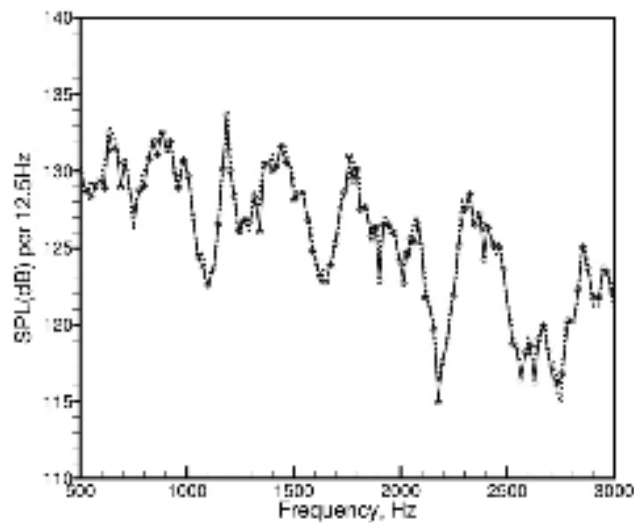
Figure 2.18. Incident sound spectrum at an OASPL of 150 dB.

Fig. 2.19. Resistance in normalized form. Solid line 600^0 K, dotted line 15^0 C. SPL=150 dB.

Fig. 2.20. Resistance in Rayl. Solid line 600^0 K, dotted line 15^0 C., SPL=150 dB.

13
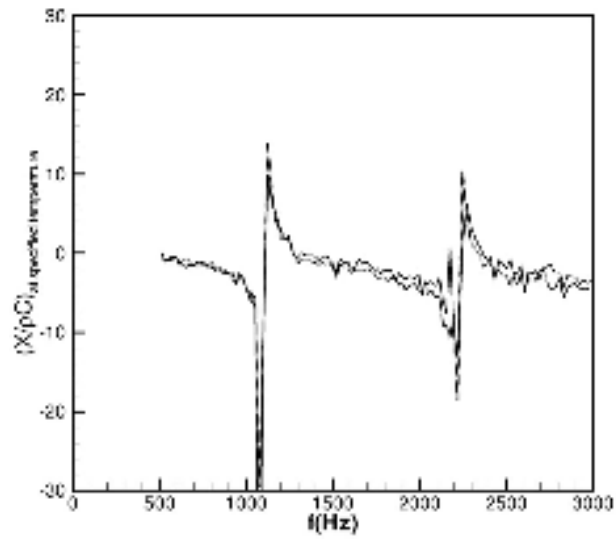
Fig. 2.21. Normalized Reactance. Solid line 600^0 K, dotted line 15^0C. SPL=150 dB.
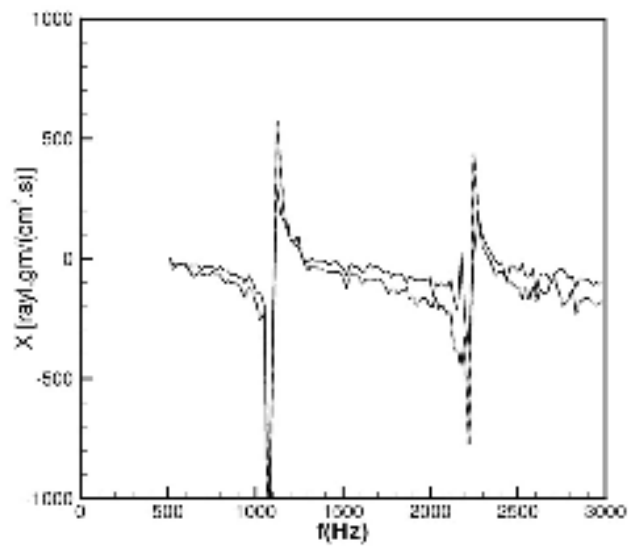
Figure 22. Reactance in Rayl. Solid line 600^0 K, dotted line 15^0 C. SPL=150 dB.

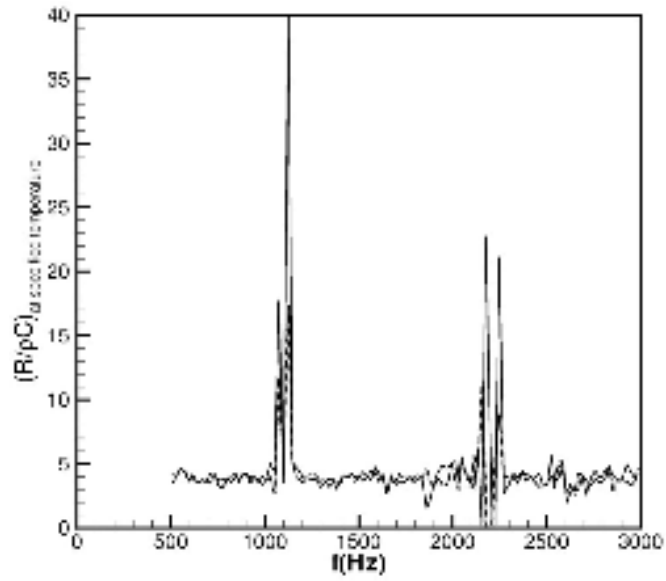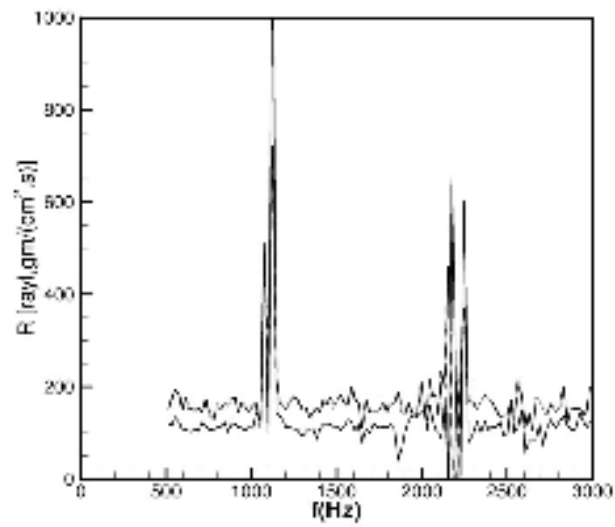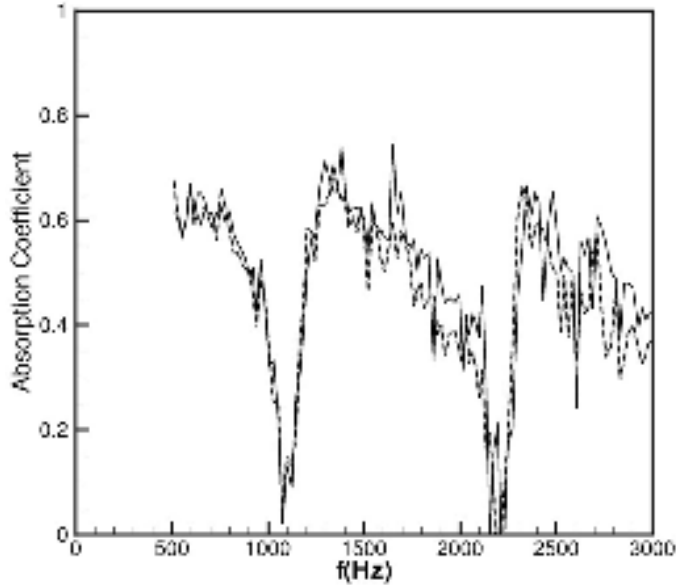Figure 23. Absorption Coefficient. Solid line 600^0 K, dotted line 15^0 C. SPL=150 dB.

B. Computational investigation of the impedance of an acoustic liner.

In our Phase I study of the impedance of a liner, an array of 10 resonators is chosen as a representative liner. This size array is adopted just for the purpose of demonstrating feasibility. Also a long array would require a much longer computing time. This would prevent us from doing a more detailed parametric study to illustrate the difference between the impedance of a liner and that of a single resonator. The difference is, of course, the result of mutual interaction among the resonators that form the liner. In our study, the liner sample is again placed at the end of a normal incidence impedance tube as shown in Fig. 2.24. Discrete incident sound at a range of SPL is used in the study. The computation is preformed at 15^0 C and at 600^0 K.
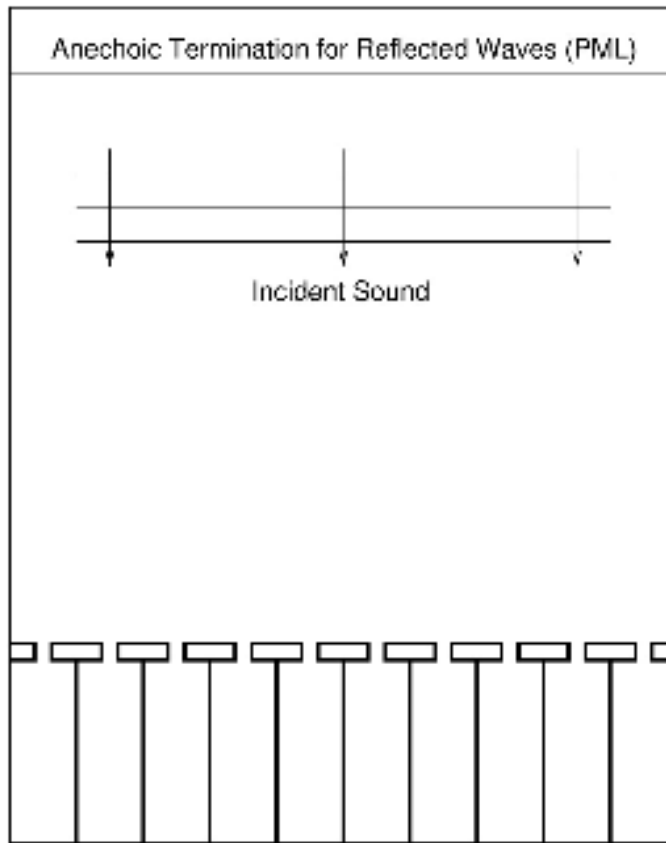
Figure 2.24. An acoustic liner sample consisting of 10 resonators housed in a normal incidence impedance tube. Each resonator is the same as that in Fig. 3 & Fig. 4.

Because 10 resonators are used in the liner sample, the width of the impedance tube is 10 times wider than that for a single resonator. This larger width allows the propagation of high order duct modes in the impedance tube. In contrast, the narrower impedance tube for a single resonator would only allow the propagation of the plane wave mode for frequencies up to 6 kHz. In our Phase I study, the first three propagating modes (n = 0, 1, 2 ; n = mode number) are used as incident wave. The n = 1 and 2 modes may be regarded as representing conditions under which the incident sound pressure on the liner is not uniform. This is typical of what a liner would encounter in a jet engine inlet duct in the presence of upstream propagating spinning duct modes.

Instant Pressure Contours

Mode number: 0

Frequency: 2000Hz

SPL: 152dB

Temperature: 15C

10 Resonators

mode	PWL(+) dB	PWL(-) dB
0	117.93	118.95
1	77.16	75.61
2	75.36	71.67
3	74.46	81.25
4	72.76	71.75
5	73.06	76.06
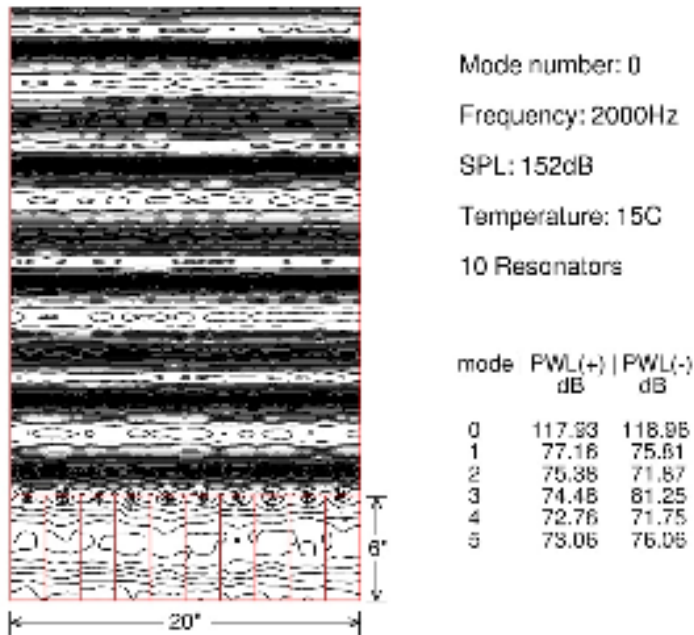
Figure 2.25. Instantaneous pressure contours inside the impedance tube. n=0 mode.

Figure 2.25. shows the instantaneous pressure contours inside the normal incidence impedance tube with incident sound in the n = 0 mode at 2 kHz, 152 dB SPL and 15^0 C. The energy flux (PWL) based on Morfey's formula of all the propagating modes are calculated from the simulation data. The table adjacent to the figure lists the magnitude in dB. PWL(-) are the incident modes. PWL(+) are the reflected modes. It is clear from the table, the sound field is dominated by the n = 0 mode, the mode of the incident wave.

Instant Pressure Contours

Mode number: 1

Frequency: 2000Hz

SPL: 152dB

Temperature: 15C

10 Resonators

mode	PWL(+) dB	PWL(-) dB
0	75.96	71.56
1	115.10	115.83
2	76.56	76.54
3	83.37	73.80
4	72.63	73.18
5	65.61	60.81

17
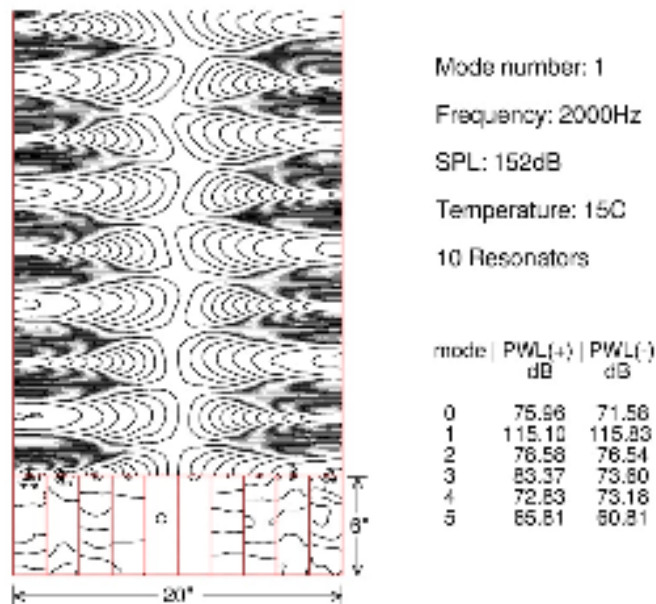
Figure 2.26. Instantaneous pressure contours inside the impedance tube. n=1 mode.

Instant Pressure Contours

Mode number: 2

Frequency: 2000Hz

SPL: 152dB

Temperature: 15C

10 Resonators

mode	PWL(+) dB	PWL(-) dB
0	69.08	29.94
1	77.50	73.09
2	115.07	115.60
3	77.97	69.85
4	66.39	62.99
5	77.17	76.60
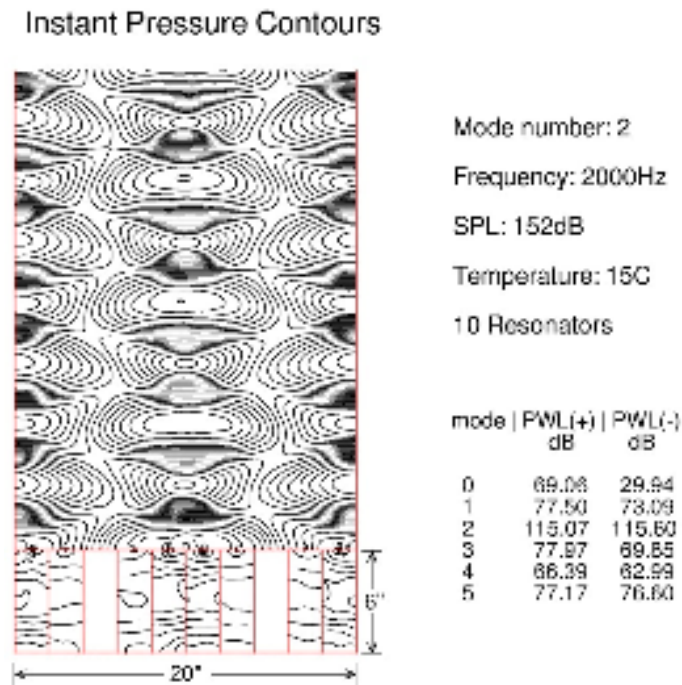
Figure 27. Instantaneous pressure contours inside the impedance tube. n=2 mode.

Fig. 2.26 and Fig. 2.27 show the results of similar computation for the n = 1 and 2 incident modes. The instantaneous pressure contours show the standing sound wave pattern inside the impedance tube. However, inside the liner, because the internal partitions prevent lateral fluid motion, the pattern is slightly different. Still the computed PWL values indicate that waves with the same mode number as the incident wave dominate the sound field.

18

Instant Pressure Contours
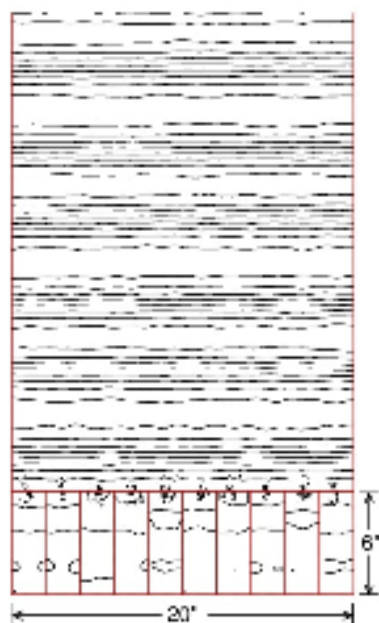
Mode number: 0

Frequency: 1500Hz

SPL: 146dB

Temperature: 15C

10 Resonators

mode	PWL(+) dB	PWL(-) dB
0	110.31	112.94
1	67.43	65.05
2	65.20	43.87
3	49.17	71.43
4	68.61	55.59

6"

20"

Figure 2.28. Instantaneous pressure contours inside the impedance tube. n=0 mode.

Instant Pressure Contours
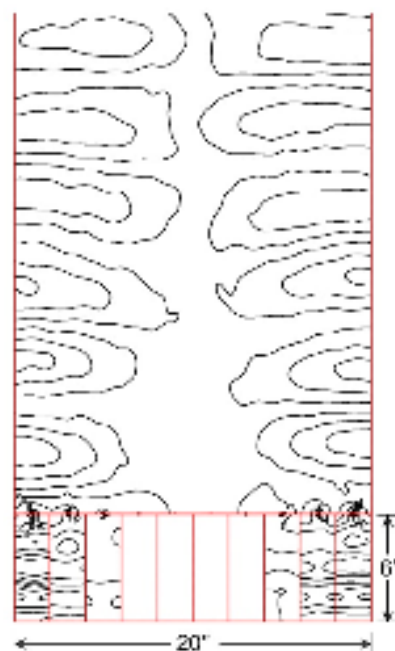
Mode number: 1

Frequency: 1500Hz

SPL: 146dB

Temperature: 15C

10 Resonators

mode	PWL(+) dB	PWL(-) dB
0	54.48	63.61
1	107.70	109.81
2	62.74	65.09
3	86.71	63.43
4	58.92	63.10

6"

20"

Figure 2.29. Instantaneous pressure contours inside the impedance tube. n=1 mode.

Instant Pressure Contours

Mode number: 2

Frequency: 1500Hz

SPL: 146dB

Temperature: 15C

10 Resonators

mode	PWL(+) dB	PWL(-) dB
0	48.05	53.14
1	67.36	69.57
2	107.15	109.46
3	65.01	67.30
4	61.05	54.62

Figure 2.30. Instantaneous pressure contours inside the impedance tube. n=2 mode.

Figs. 2.28, 2.29 and 2.30 are computations similar to those of Figs. 2.25 to 2.27 but at a frequency of 1.5 kHz. They provide further confirmation of the observation that waves with the same mode number as the incident wave dominate the sound field inside the impedance tube.
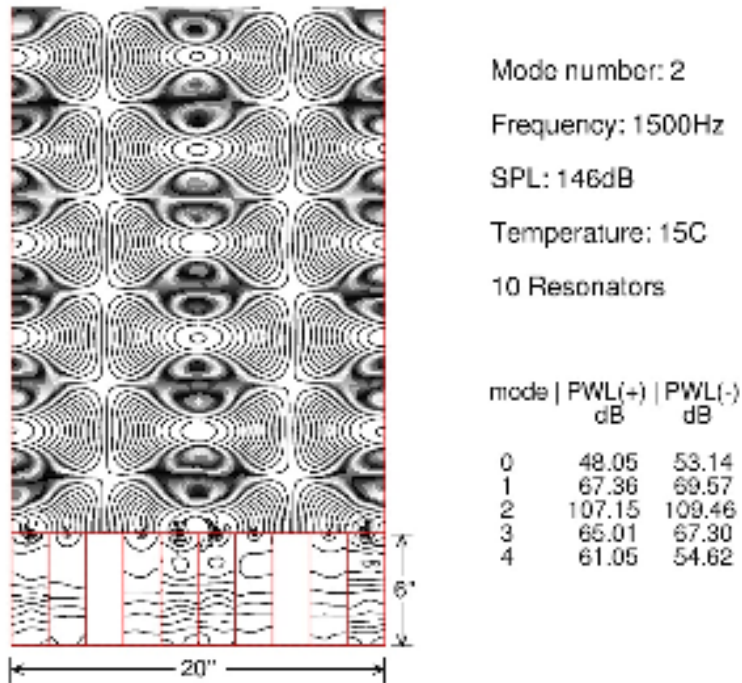
The observation that essentially only waves of one wave mode number form the standing wave pattern inside the impedance tube allows the use of the two-microphone method to measure and compute the liner impedance. In this way, we determine the acoustic impedance of a liner under non-uniform incident sound. It is to be noted that if this impedance is not the same as that of a single resonator then it is a strong indication that there is mutual acoustic interaction between neighboring resonators of a liner.
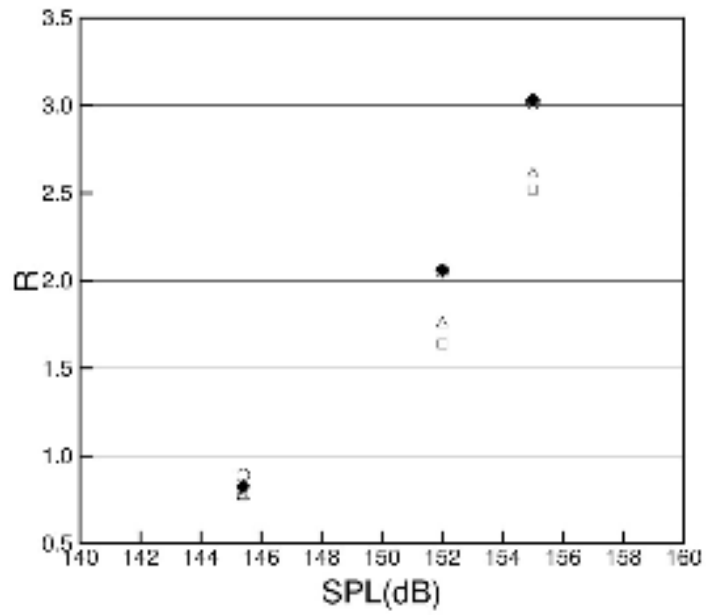
Fig. 2.31. Resistance of liner at 2 kHz. ◆ single resonator. ○, △, □, mode 0, 1, 2.
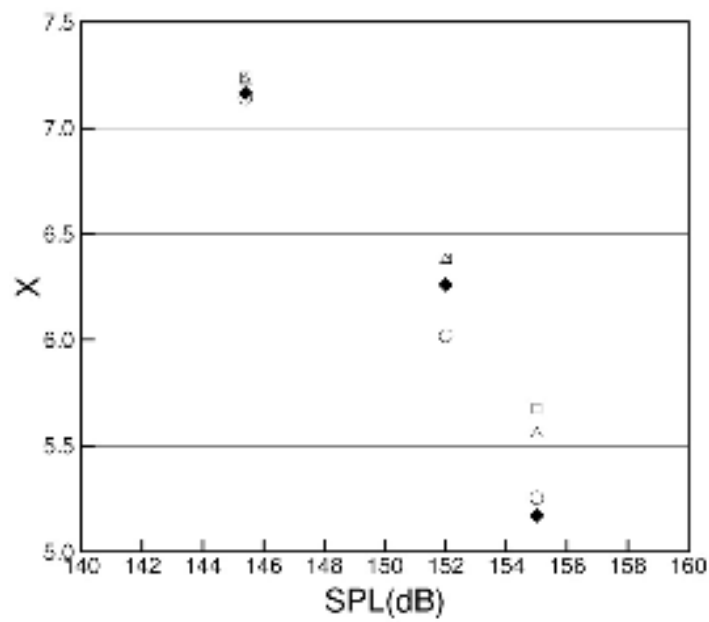
Fig. 2.32. Reactance of liner at 2 kHz. ◆ single resonator. ○, △, □, mode 0, 1, 2.
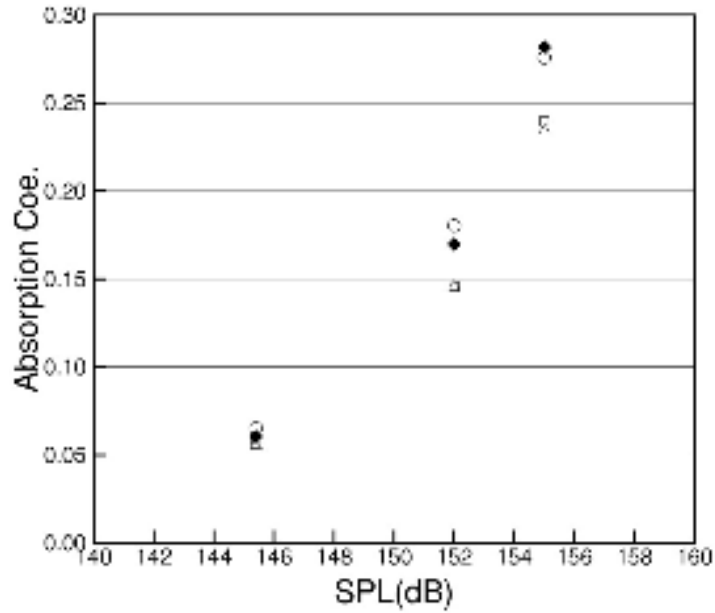
Fig. 2.33. Absorption Coeff. at 2 kHz. ◆ single resonator. ○, △, □, mode 0, 1, 2.

Figs. 2.31, 2.32 and 2.33 show the resistance, reactance and absorption coefficient of the liner at 2 kHz frequency when the incident waves have mode number 0, 1, and 2. Shown also are the corresponding results of a single resonator. These results suggest that as SPL increases, the impedance and absorption coefficient of a liner under high order mode incident waves deviate increasingly from those of a single resonator. Fig. 34, 35 and 36 show similar liner acoustic behavior at an incident sound wave frequency of 1.5 kHz. At this time, we are unaware that the effect of non-uniform SPL on the impedance of a liner has been investigated before. The present result is believed to be new. This study is, however, only preliminary. Further work is needed to determine its significance.

Fig. 2.34. Resistance of liner at 1.5 kHz. ◆ single resonator. ○, △, □, mode 0, 1, 2.

22

Fig. 2.35. Reactance of liner at 1.5 kHz. ♦ single resonator. ○, △, □, mode 0, 1, 2.

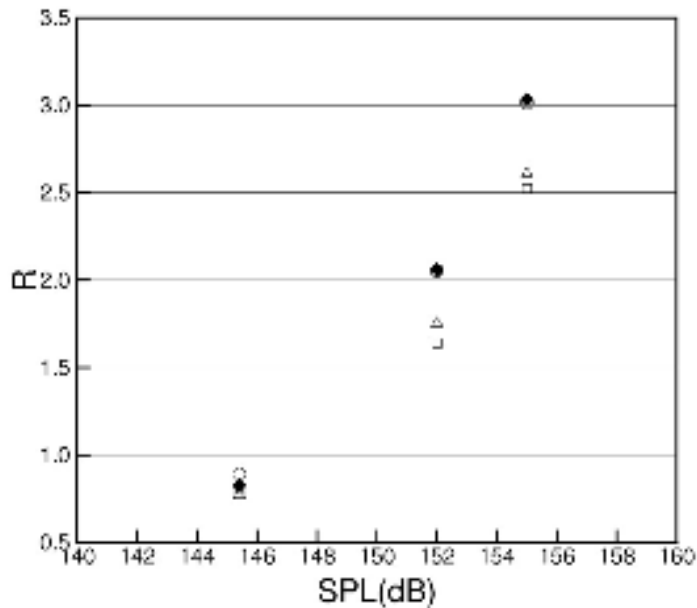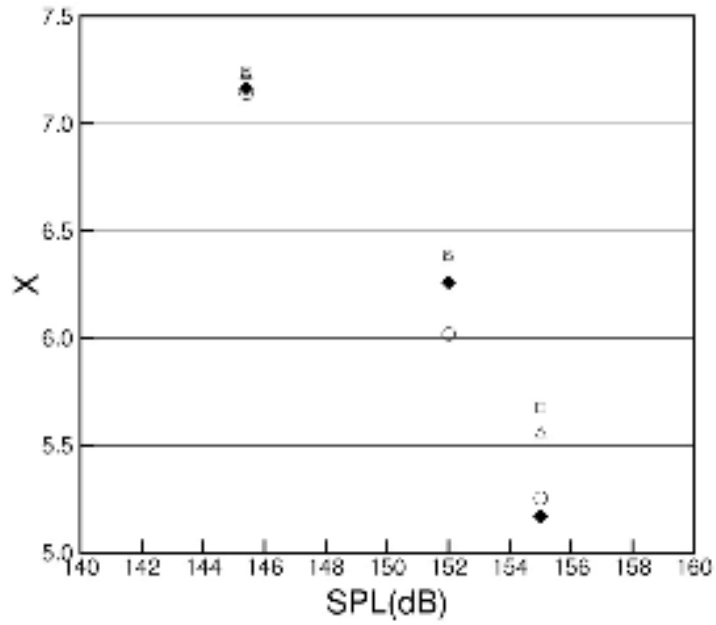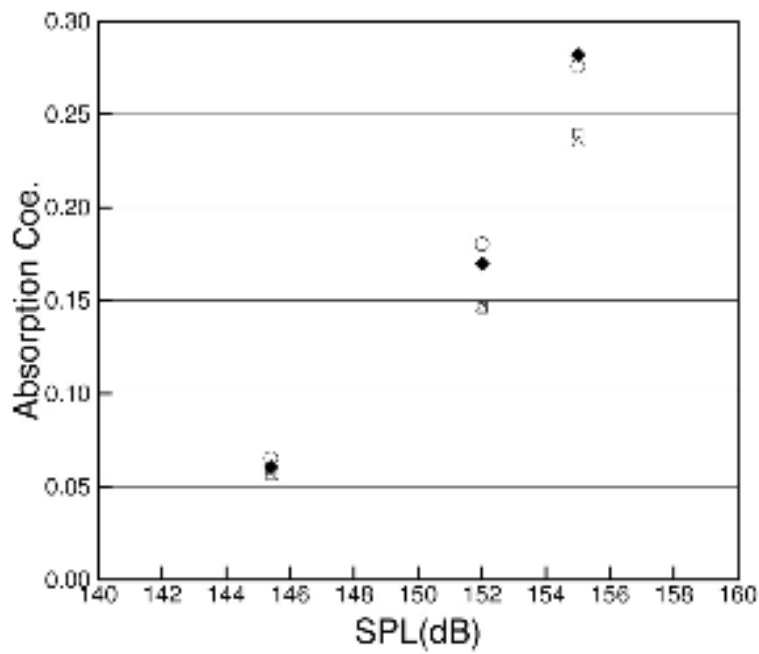Fig. 2.36. Absorp Coeff. of a liner at 1.5 kHz. ♦ single resonator. ○, △, □, mode 0, 1, 2.

3. GRAZING FLOW IMPEDANCE MODEL FOR SERIES COUPLED HELMHOLTZ RESONATORS

An axial (1-DOF) control volume model was developed to predict the impedance of series coupled Helmholtz resonators constructed with circular orifices exposed to high amplitude sound and uniform grazing flow. The model addresses only the effects of resonator geometry, incident sound pressure amplitude and *uniform* grazing flow. It does not include the effects of grazing flow boundary-layer thickness. Non-linear modeling is restricted to the front cavity. Predicted impedances show good agreement with NASA furnished data over a wide range of grazing flow speeds, sound pressure amplitudes and frequencies.

Model Derivation

The derivation of the impedance prediction model is based on applying conservation of unsteady mass and *vertical* momentum across the control volume sketched in Figure 3.1. The quantities "1" and "2" denote the front and rear cavities, respectively. During the in-flow half-cycle, the acoustic volume flow entering the front cavity orifice upper control surface is denoted by $u_o S_1$. The quantity $u_{vc} S_{vc}$ represents the sound particle volume flow exiting the front cavity control volume lower surface, where S_{vc} represents the so-called "vena contracta" area. The volume flow VS_V represents the grazing volume flow deflected into the front control volume by the driving sound pressure field P_o. The quantities H_1/H_2, τ_1/τ_2 and L_1/L_2 represent the front/rear orifice inertial lengths, faceplate thicknesses *and* cavity depths respectively. Finally, τ_{w1} and τ_{w2} represent the viscous resistive losses on the front/rear faceplate thickness wetted areas, respectively.

The in-flow model is valid only during the half-cycle when the incident acoustic velocity is pumped into the resonator cavity - it is not valid during the other half-cycle when the acoustic velocity is ejected from the resonator cavity. This restriction is not unduly limiting because the particle volume flow pumped into and out-of the resonator volume must be constant over a dynamically steady-state sound period. Thus an approximate solution over the in-flow half-cycle should result in an approximate solution over the entire cycle.

Conservation of Mass

Assuming $H \gg \lambda$, Tempkin has shown that to lowest order, compressibility effects are small with respect to mass flow convection[1]. With this simplification, the conservation of mass flux across the upper cavity control volume may be written, where u_o, u_{inv} and u_{BL} are understood to be functions of time, as

$$VS_v + u_o S_1 = u_{vc} S_{vc} = u_1 S_1 \qquad (3.1)$$

Here $u_1 S_1$ represents the acoustic volume flow entering the front cavity referenced to the front orifice area S_1. Equation (3.1) shows that, to the lowest order, the pumping of volume flow into and out-of the front resonator orifice is governed by unsteady, incompressible motion. This makes sense because significant acoustic changes can occur only over scale lengths on the order of an acoustic wavelength.
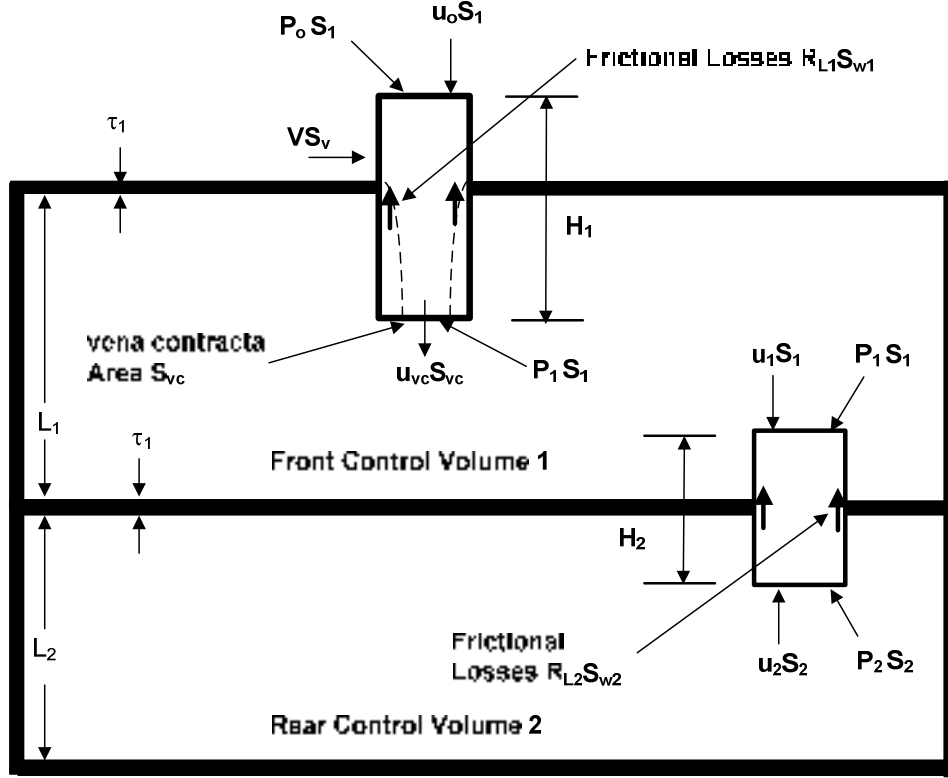
Figure 3.1. Control Volume Used in Derivation of 2-DOF Impedance Model

Front Cavity Conservation of Vertical Momentum

The conservation of momentum in the vertical direction across the front control volume is expressed as,

$$\rho_o S_1 H_1 \frac{du_1}{dt} = \rho_o \left(u_o^2 S_1 - u_{vc}^2 S_{vc} \right) + \left[P_o - P_1(L_1) \right] S_1 - \tau_{w1} S_{w1} \qquad (3.2)$$

The various terms in (3.2) are described below:

- The first term on the left-hand-side (LHS) represents the rate of increase of momentum stored in the front cavity control volume. The inertial length parameter H_1 is unknown and must be determined experimentally.

- The first term on the right-hand-side (RHS) represents the net nonlinear increase in momentum flux across the front cavity upper and lower control surfaces.

- The second term on the RHS represents the net vertical acoustic driving force acting on the control volume. Here P_0 represents the acoustic pressure driving the sound particle volume flow into the cavity during the inflow half-cycle and $P_1(L_1)$ represents the cavity restoring pressure at the orifice. Hot-wire experiments conducted by Ingard and Ising showed that orifice near-field effects extend to about two or more orifice diameters[2] Thus P_o, as defined in Figure 3.1, may not accurately represent the acoustic driving pressure during the inflow half-cycle. Possible errors in P_o will be corrected empirically using the discharge coefficient concept defined below.

- The third term on the RHS represents the momentum loss from frictional wall shear stresses τ_{W1} distributed over the face-plate thickness wetted area $S_{W1} = \pi d_1 \tau_i$.

Discharge/Grazing Flow Coefficients. Equation (3.2) is simplified by introducing an acoustic discharge coefficient C_d and a grazing flow coefficient C_V defined as,

$$C_d \equiv \frac{S_{vc}}{S_0}; \quad C_v \equiv \frac{S_v}{S_0} \tag{3.3}$$

The discharge coefficient C_d governs the average sound particle volume flow rate entering the inner resonator cavity. It is the acoustic equivalent to the discharge coefficient concept used in steady-state pipe flow[3,4]. The grazing flow coefficient C_V governs the steady-state grazing volume flow rate deflected into the inner resonator orifice.

Substituting (3.1) and (3.3) into (3.2) results in the following simplification,

$$\rho_o S_1 H_1 \frac{du_1}{dt} + \rho_o S_1 \left[\left(\frac{1-C_d}{C_d} \right) u_1^2 + 2C_V V u_1 \right] = S_1(P_o - P_1) - S_{w1}\tau_{w1} \tag{3.4}$$

In deriving (3.4), steady-state terms associated with the deflection of the grazing flow into the cavity were ignored and only acoustic terms retained. It is intuitively clear that at low values of SPL, resonator non-linear resistive losses become negligibly small. Under these conditions, the non-linear term *(1-C_d)* should also become negligibly small.

The non-linearity of (3.4) prevents an analytic solution. It must be solved numerically to achieve a dynamically steady-state solution, followed by a Fourier transform to calculate the fundamental harmonic velocity component. Although this procedure is numerically straightforward, it greatly complicates the design of sound absorbing liners. Equation (3.4) can be linearized by incorporating the experimental findings of Ingard and Ising, who used hot-wires to measure the amplitudes of higher harmonic velocity components[2]. Their measurements showed, at high SPLs, that alternating non-linear jetting into and out-of an orifice takes place during each half-cycle. Further, the higher component velocity components were small compared to the fundamental. Physically, this permits the replacement of the nonlinear term u^2 in (3.4) with the approximate expression,

$$u_1^2 \cong |u_1| u_1(t) \cong u_1^2 \, e^{i\omega t} \tag{3.5}$$

Rear Cavity Conservation of Vertical Momentum.

The conservation of momentum in the vertical direction across the rear control volume is expressed as,

$$\rho_o S_2 H_2 \frac{du_2}{dt} = (P_1 - P_2)S_2 - \tau_{w2} S_{w2} \tag{3.6}$$

Implicit in the derivation of (3.6) is the assumption that nonlinear acoustic jetting is suppressed in the rear cavity. This assumption is discussed later.

Front/Rear Cavity Pressures.

The derivation of the rear cavity pressure P_2 assumes that the cavity-area averaged acoustic volume flow $u_2\sigma_2 S_c$ enters the cavity, where S_c represents the cavity cross-sectional area and $\sigma_2 = S_2/S_c$. It is also assumed that the cavity pressure can be accurately modeled by solving the one-dimensional wave equation. The following expression is derived, where $k = \omega/c_0$,

$$P_2 = -i\rho_0 c_0 \sigma_2 \cot(kL_2) u_2 \tag{3.7}$$

26

The derivation of the front cavity pressure P_1 assumes that the acoustic volume flow $u_2\sigma_2 S_c$ exits the front cavity at x = 0 and that the acoustic volume flow $u_1\sigma_1 S_c$ enters the front cavity at x = L_1. Application of the one-dimensional wave equation yields the following solution,

$$P_1 = -i\rho_0 c_0 \sigma_1 \cot(kL_1)u_1 + i\frac{\rho_0 c_0 \sigma_2}{\sin(kL_1)}u_2 \tag{3.8}$$

Front/Rear Viscous Scrubbing Losses

The front/rear wall shear stresses τ_{w1} and τ_{w2} are assumed to be generated by steady-state and unsteady viscous scrubbing losses. A simple model, based upon dimensional analysis, is proposed. Consider the front orifice. Steady-state shear stresses are assumed to be proportional to $\mu_o u_1/\delta_{av}$ where δ_{av} is an orifice faceplate thickness averaged boundary-layer thickness. Because δ_{av} is unknown, it is assumed to be proportional to the orifice diameter so that front/rear steady-state shear stresses are proportional to $\mu_o u_1/d_1$ and $\mu_o u_2/d_2$ respectively. Front/rear acoustic shear stresses are derived assuming "Stokes-like" axially uniform diffusion of vorticity over the orifice thickness, so that they are proportional to $\mu_o u_1(\omega/\nu_o)^{1/2}$ and $\mu_o u_2(\omega/\nu_o)^{1/2}$, respectively. With these assumptions, the front wall shear stress τ_{w1} is written,

$$\tau_{w1} = \left(K_{ss1} + K_{ac1}\sqrt{\frac{\omega d_1^2}{\nu_0}}\right)\frac{\mu_o}{d_1}u_1 \tag{3.9}$$

where K_{ss1} and K_{ac1} are viscous parameters experimentally determined by Hersh, Walker and Celano to be[5],

$$K_{ss1} = 13 + 10.23\left(\frac{\tau_{w1}}{d_1}\right)^{-1.44} ; \quad K_{ac1} = 3 + 2.32\left(\frac{\tau_{w1}}{d_1}\right)^{-1} \tag{3.10}$$

The corresponding rear wall shear stress τ_{w2} is written

$$\tau_{w2} = \left(K_{ss2} + K_{ac2}\sqrt{\frac{\omega d_2^2}{\nu_0}}\right)\frac{\mu_o}{d_2}u_2 \tag{3.11}$$

Substituting (3.7-3.11) into (3.5-3.6) and dividing by $\rho_0 c_0$ yields,

$$H_1\frac{du_1}{dt} + \rho_o S_1\left(\frac{1-C_D}{C_D}\right)u_1^2 + i\frac{c_0\sigma_2}{\sin(kL_1)}u_2 + \left[2C_V V + \Gamma_1 - ic_0\sigma_1\cot(kL_1)\right]u_1 = \frac{P_o}{\rho_o} \tag{3.12}$$

and

$$\left[\Gamma_2 - ic_0\sigma_2\cot(kL_2)P_2 S_2 - i\frac{c_0\sigma_2}{\sin(kL_1)}\right]u_2 + H_2\frac{du_2}{dt} + ic_0\sigma_1 S_2\cot(kL_1)u_1 = 0 \tag{3.13}$$

Here Γ_1 and Γ_2 are introduced to simplify notation,

$$\Gamma_1 \equiv \left(K_{ss1} + K_{ac1}\sqrt{\frac{\omega d_1^2}{\nu_0}}\right)\frac{4\nu_o \tau_1}{d_1^2} \tag{3.14}$$

$$\Gamma_2 \equiv \left(K_{ss2} + K_{ac2}\sqrt{\frac{\omega d_2^2}{\nu_0}}\right)\frac{4\nu_o \tau_2}{d_2^2} \tag{3.15}$$

27

With this understanding, substituting (3.14) and (3.15) into (3.12) and (3.13) yields

$$\left\{ 2C_V V + \Gamma_1 + i\left[\omega H_1 - c_0\sigma_1 \cot(kL_1) \right] \right\} u_1$$
$$+ \left(\frac{1-C_D}{C_D} \right) u_1^2 + i\frac{c_0\sigma_2}{\sin(kL_1)} u_2 = \frac{P_D}{\rho_o} \tag{3.16}$$

$$\left\{ \Gamma_2 - i\left[\omega H_2 - c_0\sigma_2 \cot(kL_2) - \frac{c_0\sigma_2}{\sin(kL_1)} \right] \right\} u_2 + ic_0\sigma_1 \cot(kL_1) u_1 = 0 \tag{3.17}$$

Substituting (3.17) for u_2 into (3.16) yields the following expression for u_1,

$$\left(\frac{1-C_D}{C_D} \right) u_1^2 + \left\{ r_V + z_1 + \left[\frac{c^2\sigma_1\sigma_2 \cot(kL_1)}{\sin(kL_1)z_2 - ic_0\sigma_2} \right] \right\} u_1 = \frac{P_D}{\rho_o} \tag{3.18}$$

Here the quantities r_V, z_1 and z_2 are defined as

$$r_V \equiv 2C_V V; \quad z_1 \equiv \Gamma_1 + i\left[\omega H_1 - c_0\sigma_1 \cot(kL_1) \right];$$
$$z_2 \equiv \Gamma_2 + i\left[\omega H_2 - c_0\sigma_2 \cot(kL_2) \right] \tag{3.19}$$

With u_1 defined by (3.18), after some algebra, the following expression is derived for the impedance of a series-coupled 2-DOF resonator,

$$\frac{Z}{\rho_o c_0} \equiv \frac{P_D}{\rho_o c_0 \sigma_1 u_1} = 0.5\left[R_v + Z_1 + \frac{\cot(kL_1)}{\sin(kL_1)Z_2 + i} \right] + \sqrt{ R_{NL}^2 + 0.25\left[R_v + Z_1 + \frac{\cot(kL_1)}{\sin(kL_1)Z_2 + i} \right]^2 } \tag{3.20}$$

The terms R_{rad}, R_V, Z_1 and Z_2 in (3.20) are defined below as,

$$R_{NL}^2 = \left(\frac{1-C_D}{C_D} \right) \frac{P_D}{(\rho_o c_0 \sigma_1)^2}; \quad R_V = \frac{r_V}{\sigma_1 c_0} = \frac{C_V V}{\sigma_1 c_0}; \quad R_{rad} = \frac{1}{\sigma_1}\left[1 - 2\frac{J_1(kd_1)}{kd_1} \right]$$

$$z_1 = R_1 + iX_1 = R_{1corr}\frac{\Gamma_1}{\sigma_1 c_0} + i\left[\frac{\omega H_1}{c_0\sigma_1} - \cot(kL_1) \right] \tag{3.21}$$

$$z_2 = R_2 + iX_2 = R_{2corr}\frac{\Gamma_2}{\sigma_1 c_0} + i\left[\frac{\omega H_2}{c_0\sigma_2} - \cot(kL_2) \right]$$

In (3.21), the coefficient C_V includes the factor 2 and the coefficients K_{ss} and K_{ac} include the factor 4 shown in (3.14) and (3.15).

Model Validation

The predicted impedance was compared to data furnished by NASA LaRC. Table 3.1 below summarizes the 2-dof resonator configurations. Figure 3.2 summarizes the measured vs. predicted non-grazing flow dimensional resistances of Configurations # 1-8 at SPL = 140 dB. The model parameters were selected to force agreement with data.

Table 3.I. Summary of NASA Furnished 2-DOF GEAT0 Resonator Configurations

| Config	Front Cavity				Rear Cavity			
	Hole Pattern	Hole Diamter (in)	Sheet Thickness (in)	Cavity Depth (in)	Hole Pattern	Hole Diamter (in)	Sheet Thickness (in)	Cavity Depth (in)
1	4x4	0.12250	0.0625	0.46	4x4	0.12250	0.0625	0.81
2	4x4	0.12250	0.0625	0.46	4x4	0.12250	0.0125	0.81
3	4x4	0.12250	0.0625	0.46	4x4	0.12250	0.2500	0.81
4	4x4	0.12250	0.0625	0.46	4x4	0.12250	0.3750	0.81
5	16x16	0.03125	0.0625	0.46	16x16	0.03125	0.0625	0.81
6	16x16	0.03125	0.0625	0.46	16x16	0.03125	0.0125	0.81
7	16x16	0.03125	0.0625	0.46	16x16	0.03125	0.2500	0.81
8	16x16	0.03125	0.0625	0.46	16x16	0.03125	0.3750	0.81
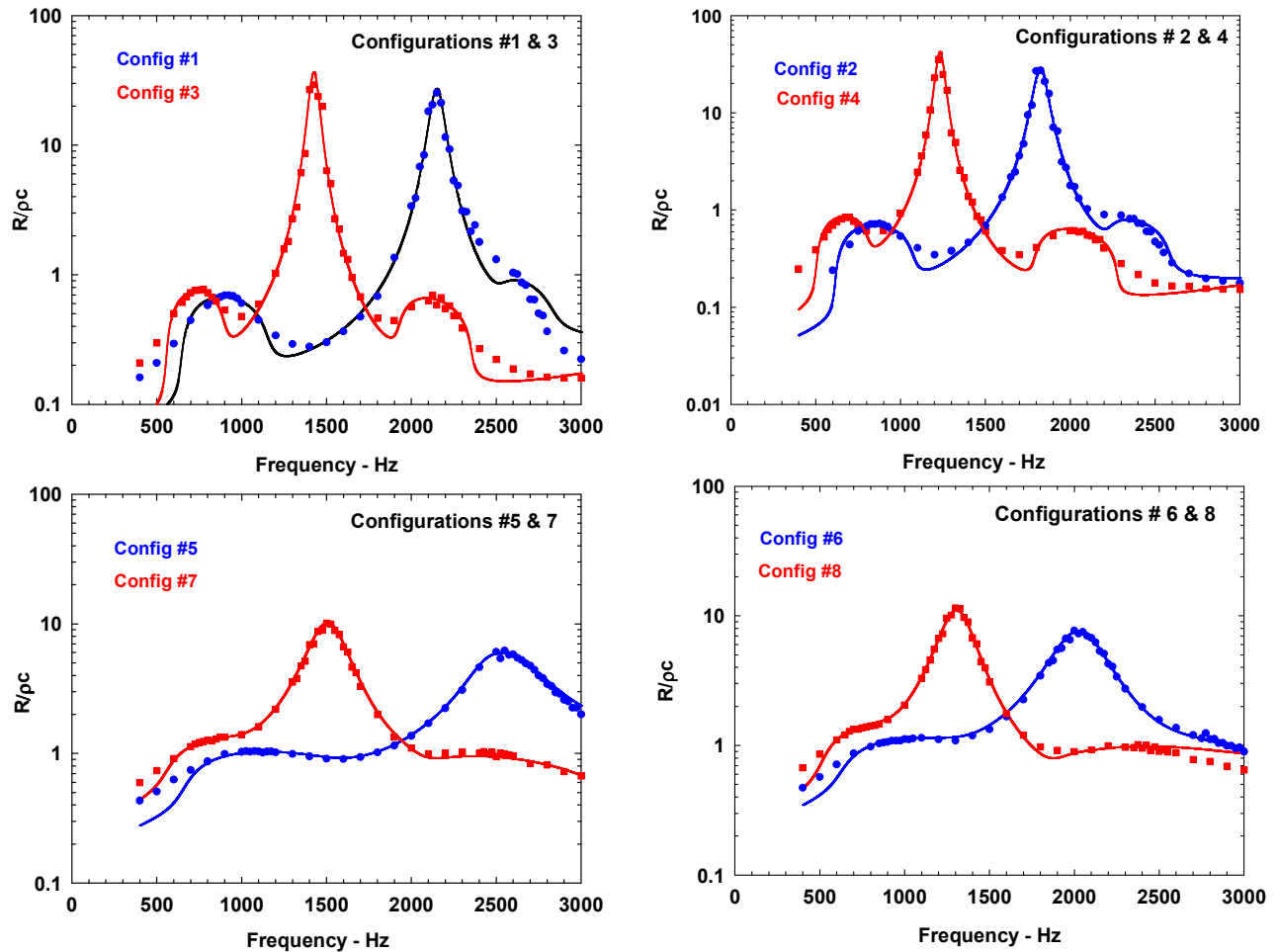
Figure 3.2. Measured and Predicted Non-Grazing Flow Resistance of Configurations # 1-8: SPL = 140 dB

Although not obvious from a casual inspection of (3.20), the impedance of the lower cavity plays a major role in controlling the resonator overall impedance. The model is attractive because the effects of grazing flow are accounted for in the continuity equation (3.1) as a mass addition. It does not explicitly affect the momentum equation (3.2) because it does not directly affect the transfer of *vertical* momentum flux in the control volume.

4. SLIT RESONATOR IMPEDANCE MODEL

An axial (1-dof) control volume model was developed to predict the impedance of Helmholtz resonators constructed with high aspect ratio rectangular slit orifices exposed to intense sound. The model addresses only the effects of resonator geometry, incident sound pressure amplitude and frequency. It does not include the effects of grazing flow.

The derivation of the slit resonator impedance model is quite similar to that derived in Section 3 for the 2-dof circular orifice coupled resonator model with the circular orifices replaced with a slit orifice. For this reason, a detailed derivation is not presented.

<u>NASA Impedance Data</u>

Figures 4.1-4.6 below summarize NASA's impedance measurements and slit goemetries for configurations S01-S32. Figure 4.7a displays the impedances of the above configurations at SPL = 120 dB. The impedance data, displayed in Figure 4.7a, exhibits the well-known sensitivity of resistance to SPL in contrast to the insensitivity of reactance. Note that the very high max/min peaks are generated at the liner anti-resonances. At roughly 1,000 Hz, the reactance curve reaches a local maximum followed immediately by a local minimun, then reaches a maximum slightly below 1,100 Hz. The corresponding resistance data displays a minimum, followed almost immediately by a maximum, then somewhat later (in frequency space) followed by a maximum. The shapes of the resistance and reactance data of all the configurations are remarkably similar even though the slit geometries range from two-dimensional (S01) to three-dimensional (S06). This is clearly shown in Figure 4.b, which compares the impedances of configurations S01 and S32. As shown clearly in all the figures, *there is a clear and unambiguous correlation between the local minimums and maximums* of the reactances and resistances.

An examination of Figures 4.1-4.7 suggest the following.

- The magnitude of the local minimums and maximums of the resistance data shown in Figure 4.1b increase with increasing SPL suggesting that *non-linearity may be the principal mechanism generating this behavior.* This may not eliminate the importance of viscosity, but it does suggest that its principal role may only be to reduce the magnitude of the acoustic velocity near the side walls housing the slits. Assuming that only harmonic sound is generated, it is well known that acoustic non-linearity generates both double frequency components (positive or additive interaction) as well as steady-state or acoustic streaming (negative or cancellation interaction). It is also well known that separation bubbles form during the inflow/outflow half-cycles as the acoustic volume flow turns into/out-of the slit. it is proposed that the bubble size is perturbed or modulated during the acoustic inflow/out-of slit acoustic volume flow to be perturbed. This, in turn, modulates the slit resistance and reactance. The data suggests that the amplitude of the separation bubble modulation increases as the amplitude of the incident acoustic pressure increases.

- The same behavior described above takes place for all slit geometries tested – ranging from 2-dof to 3-dof - suggesting that slit geometry plays only a very minor role, if any, in explaining the existence of the maximums and minimums. This was supported in Section 3 above which showed the existence of local maximums in the reactance data of 2-dof resonators constructed with multiple circular orifices in grazing flow.
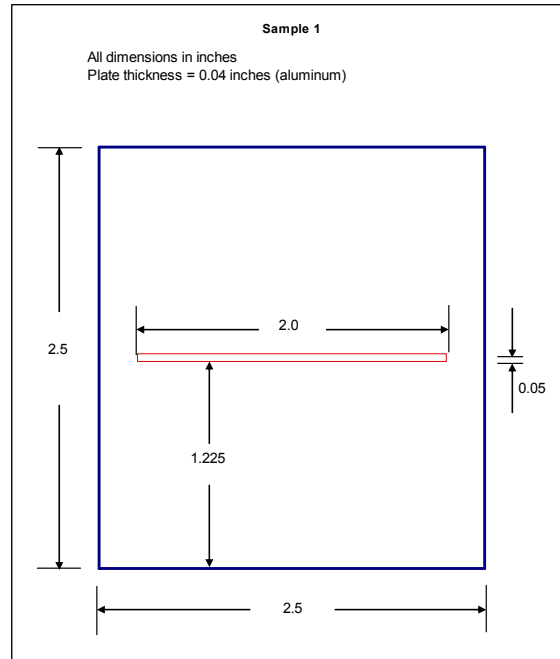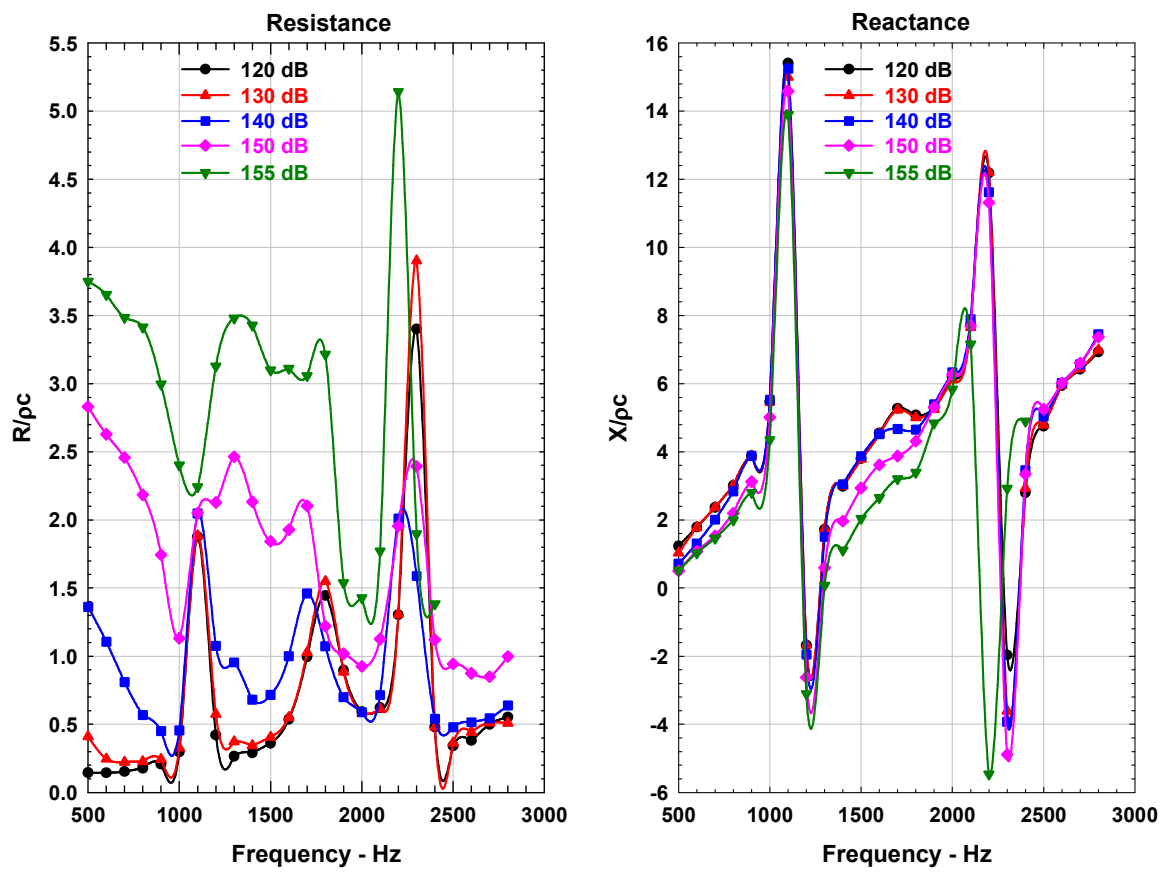
Figure 4.1a. Geometry of Sample 1

Figure 4.1b. Non-Dimensional Resistance and Reactance Data: Configuration S01
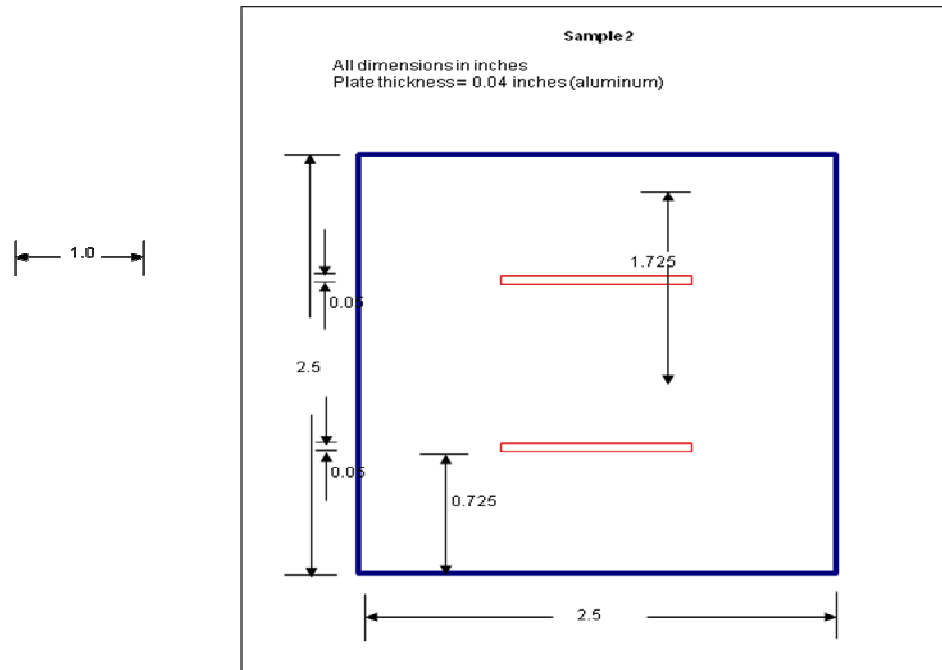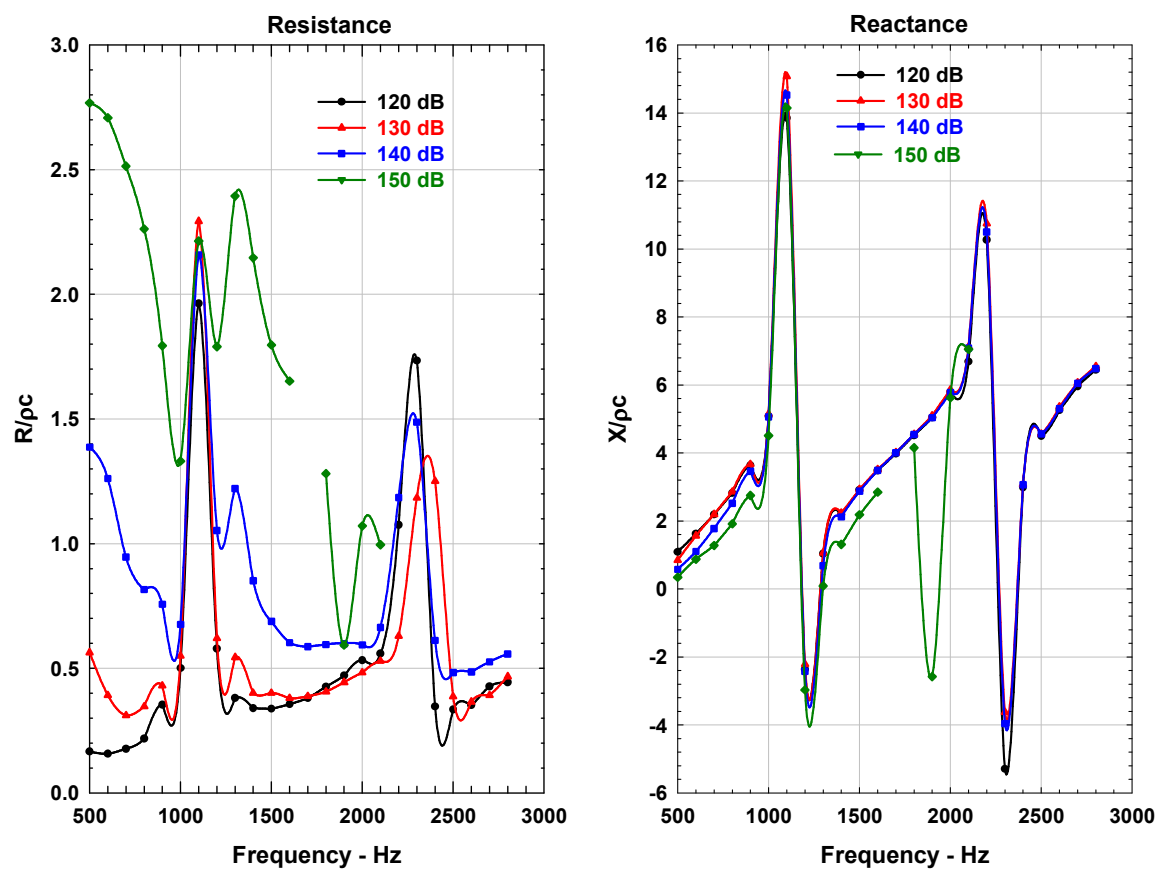
Figure 4.2a. Geometry of Sample 2

Figure 4.2b. Non-Dimensional Resistance and Reactance Data: Configuration S02
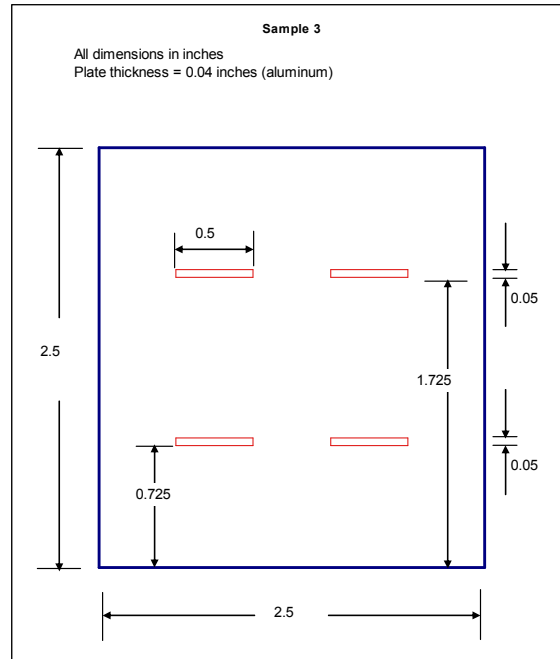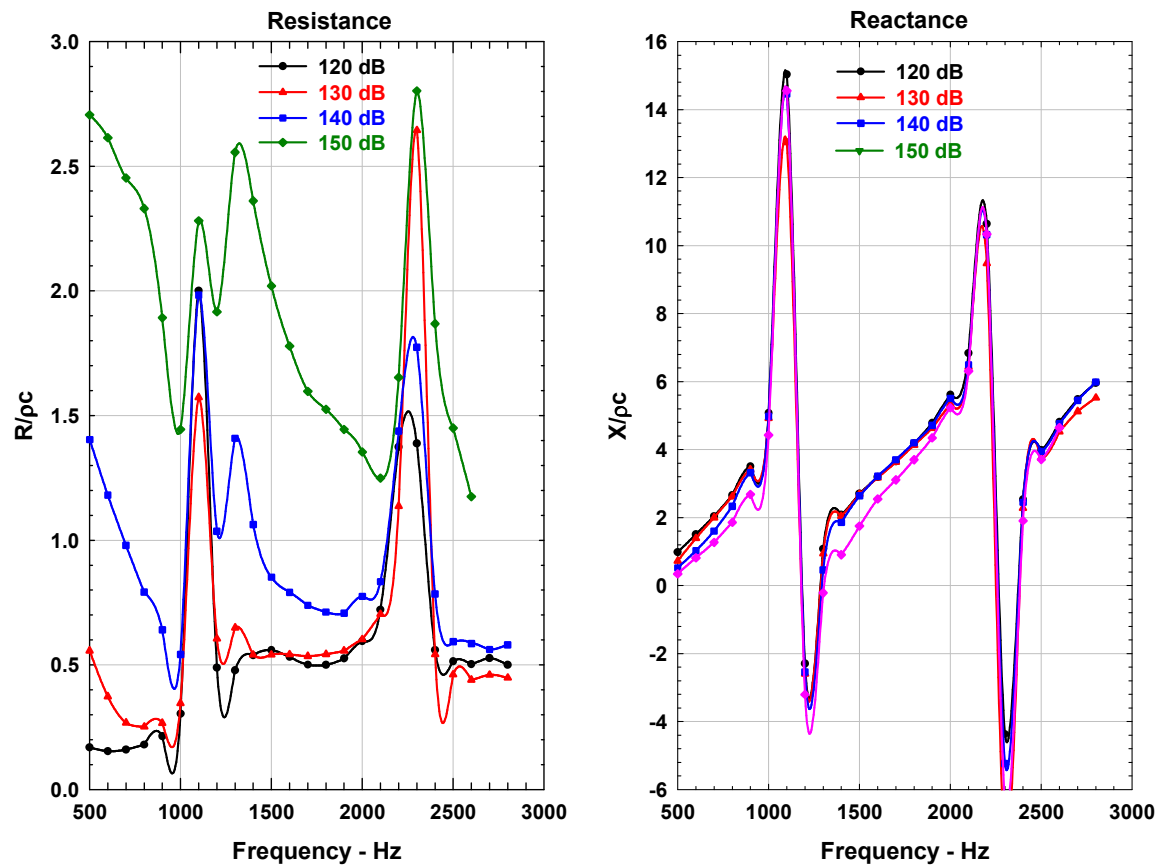
Figure 4.3a. Geometry of Sample 4

Figure 4.3b. Non-Dimensional Resistance and Reactance Data: Configuration S04
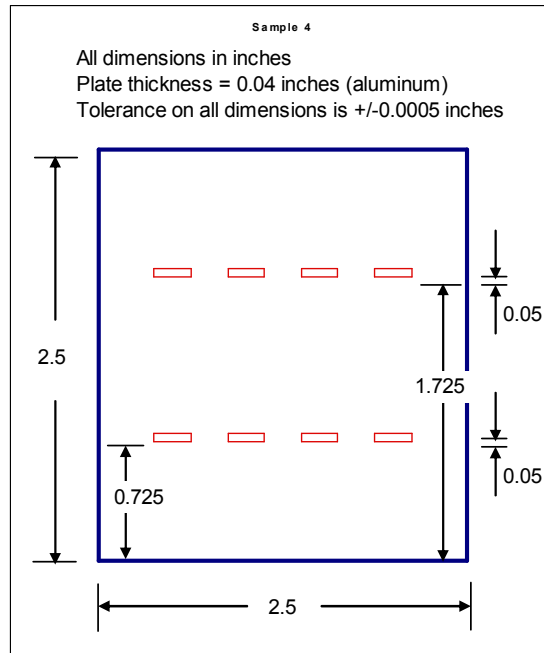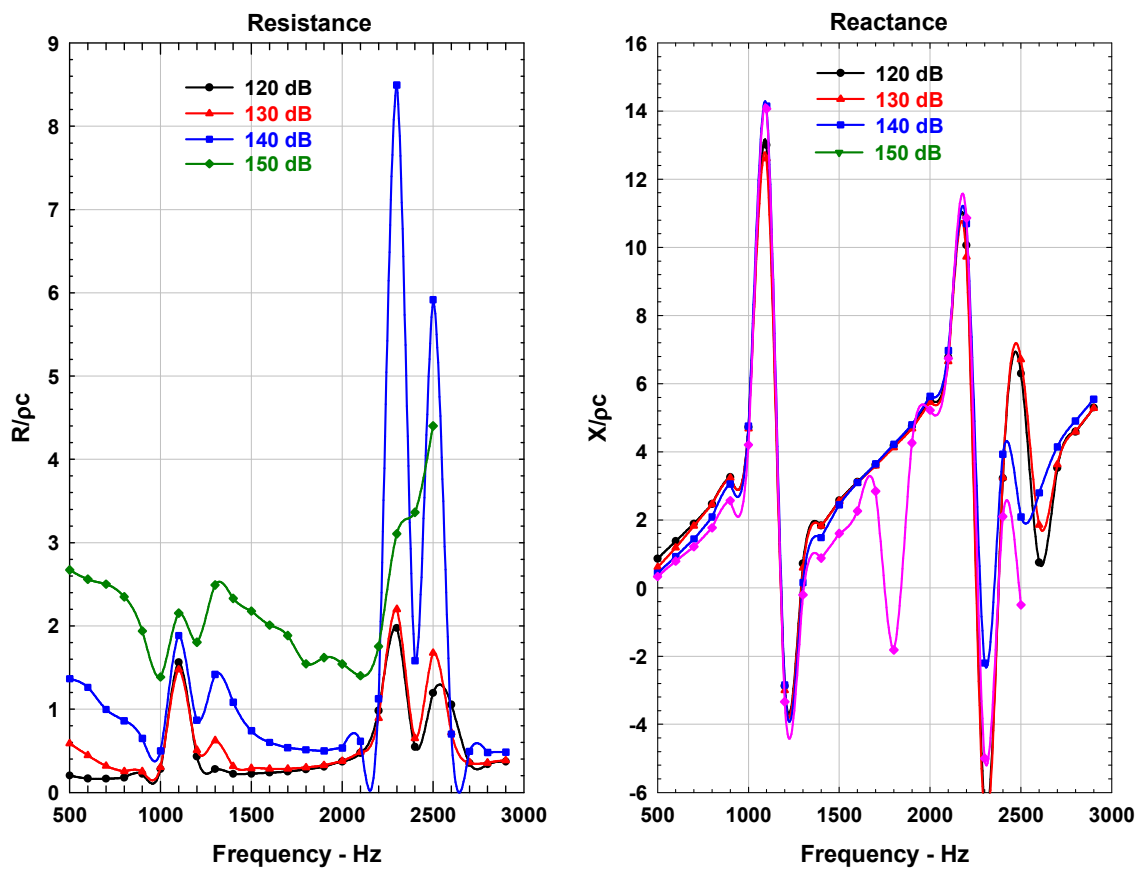
Figure 4.4a. Geometry of Sample 8

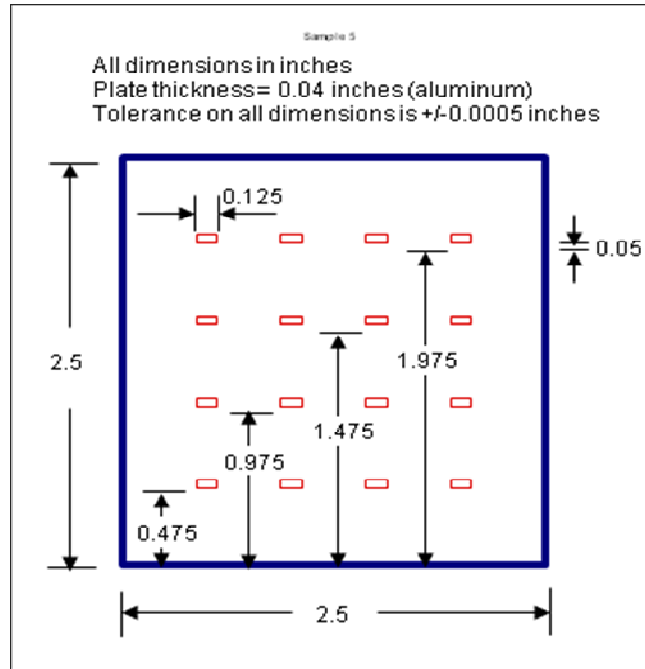Figure 4.4b. Non-Dimensional Resistance and Reactance Data: Configuration S08
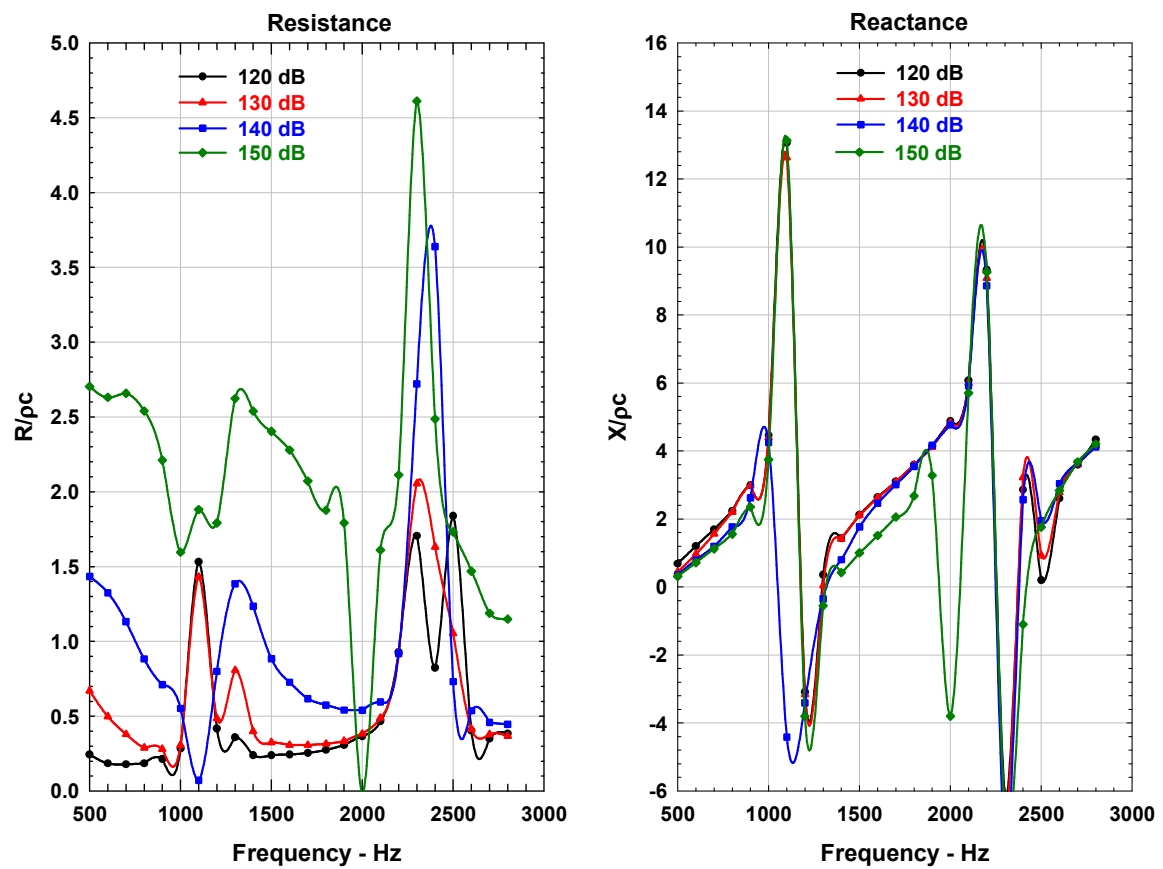
Figure 4.5a. Geometry of Sample 16

Figure 4.5b. Non-Dimensional Resistance and Reactance Data: Configuration S16
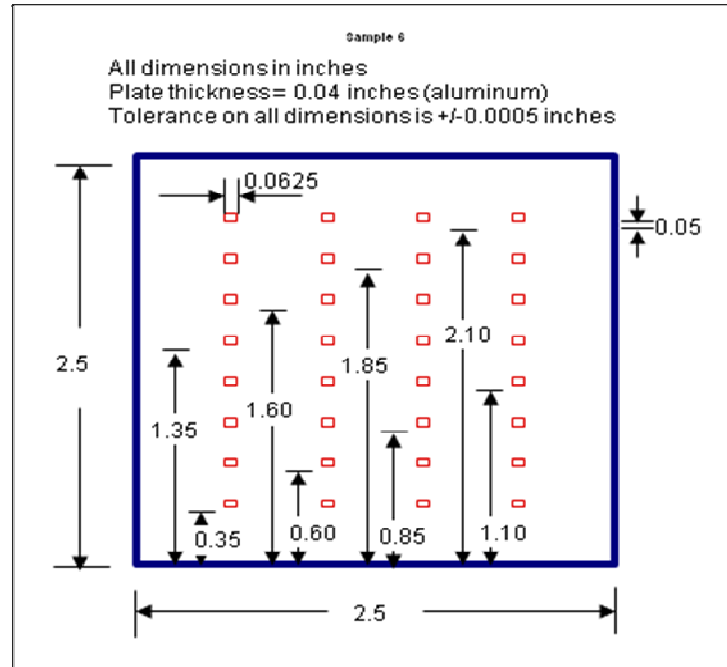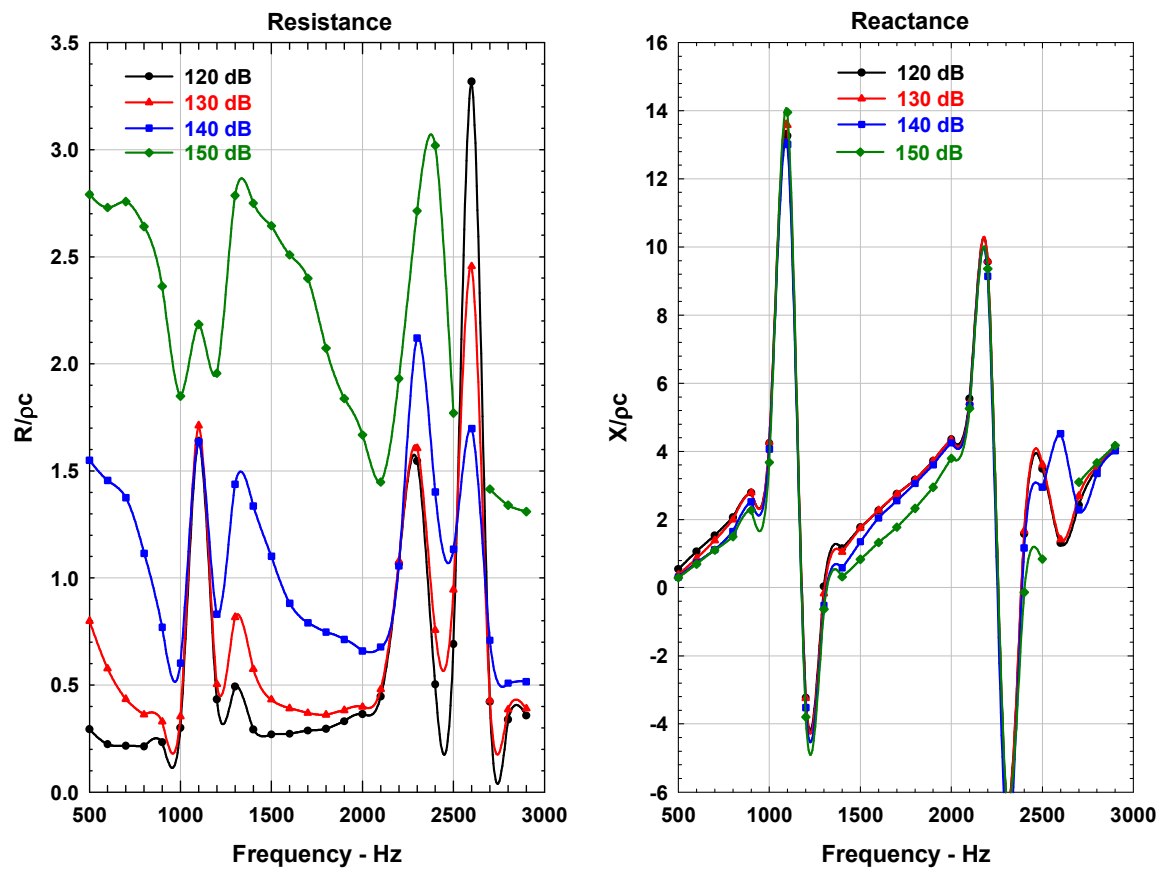
Figure 4.6a. Geometry of Sample 32

Figure 4.6b. Non-Dimensional Resistance and Reactance Data: Configuration S32
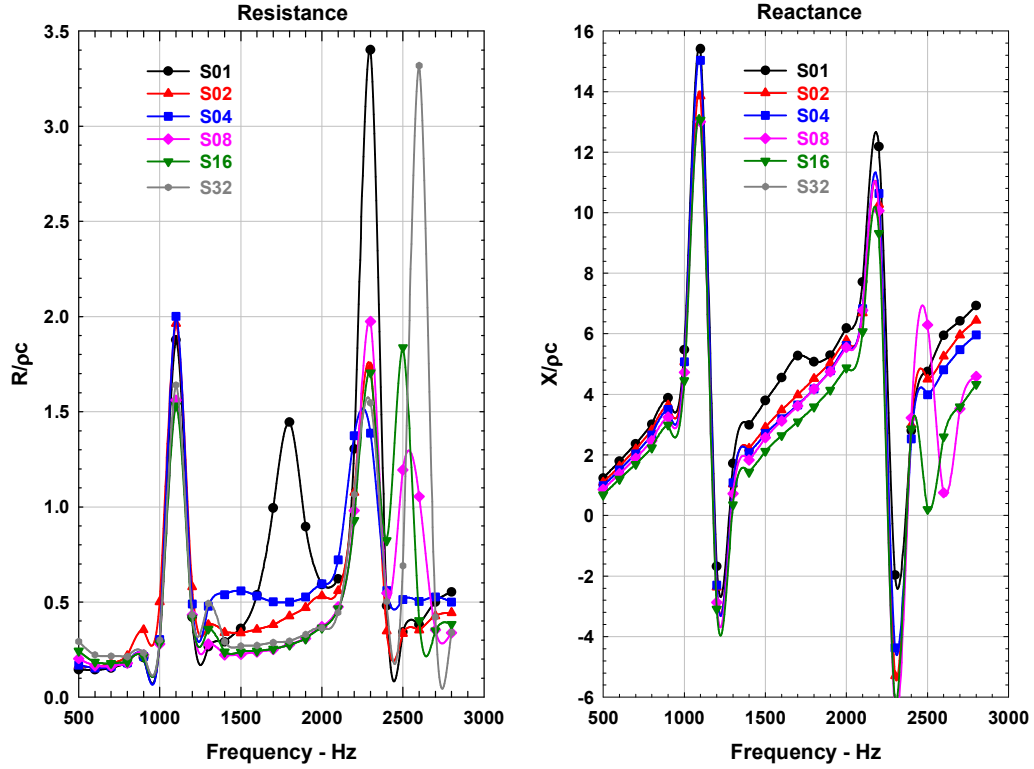
Figure 4.7a. Summary of Non-Dimensional Resistance and Reactance Data: Configurations: All Configurations, S01-S32, SPL = 120 dB
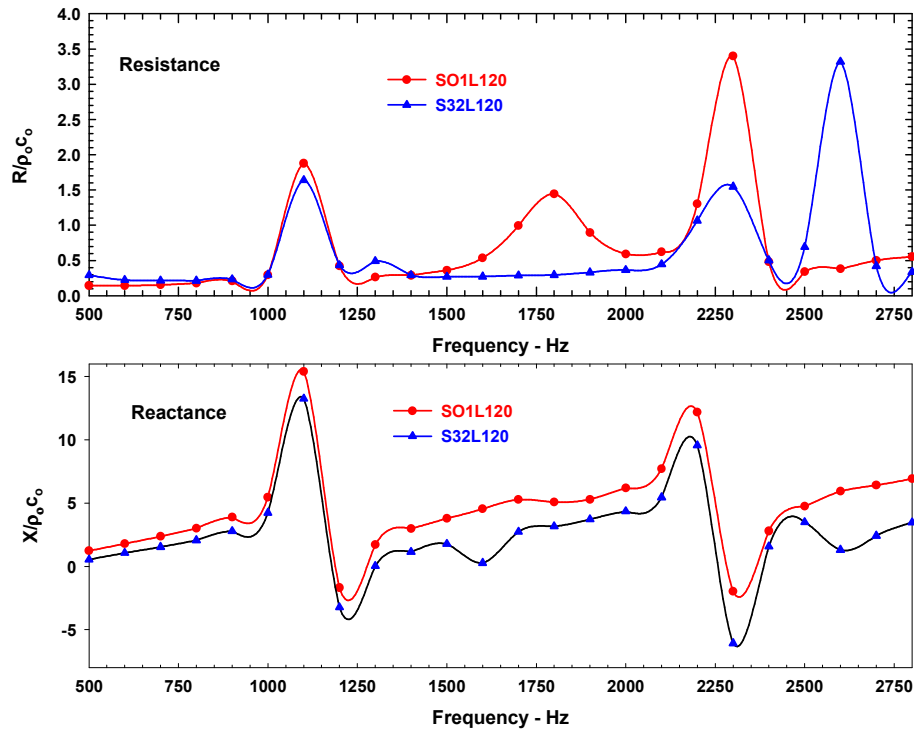

Figure 4.7b. Summary of Non-Dimensional Resistance and Reactance Data: Configurations: S01 and S32, SPL = 120 dB

<u>Model Validation.</u>

Figures 4.8a and 4.8b display measured and predicted resonator resistance and reactance of slit resonator S01L120. Figure 4.8c displays the slit model acoustic discharge coefficient, C_d, required to match the model to the measurements. Observe the rather small values of C_d required to achieve reasonable agreement between model prediction and measurements at/near resonance frequencies. Borrowing from the steady-state definition of the discharge coefficient C_d is defined as the ratio of the actual acoustic volume flow pumped into and out-of the slit resonator cavity during each half-cycle to the ideal inviscid acoustic volume flow. As showed in Figure 4.9, Johanson measured very low values of steady-state discharge coefficient of sharp-edged circular orifices at very low Reynolds numbers[6]. Unfortunately, the acoustic Reynolds numbers, R_e, characteristic of the resonator geometry, and fluid properties shown below are way too high, $R_e = 1,350$ ($W_s = 0.124$ cm, f = 2000 Hz, $\nu = 0.15$ cm^2/sec), to support the very low values of C_d. required in Figure 4.8c. This prompted the derivation of the radial control volume impedance model of the slit resonator described below.
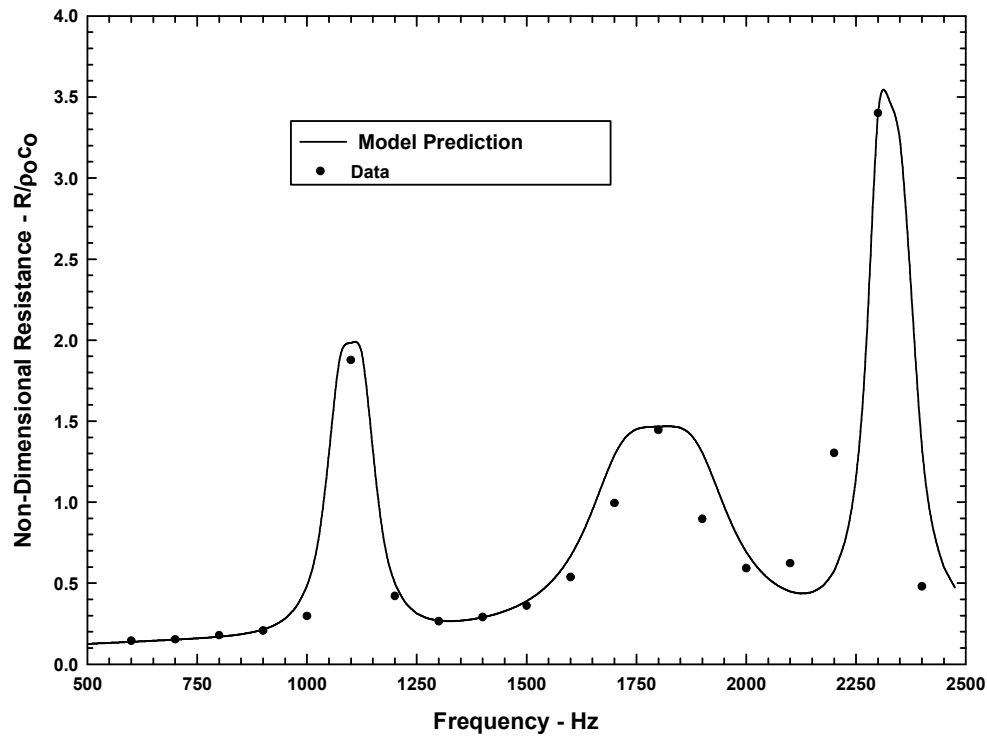

Figure 4.8a. 1-DOF Impedance Model Predicted vs. Measured Resistance: SPL = 120 dB, Configuration S01L120; K = 1.1, H/Ws = 3.20
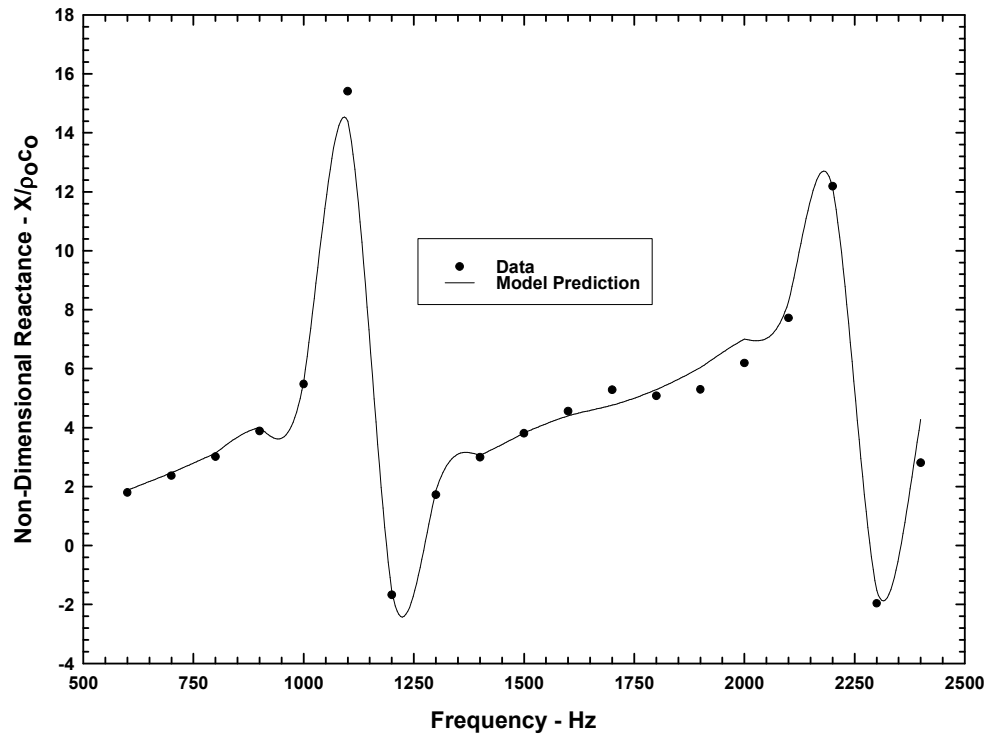
Figure 4.8b. 1-DOF Impedance Model Predicted vs. Measured Reactance: SPL = 120 dB, Configuration S01L120; K = 1.1, H/Ws = 3.20
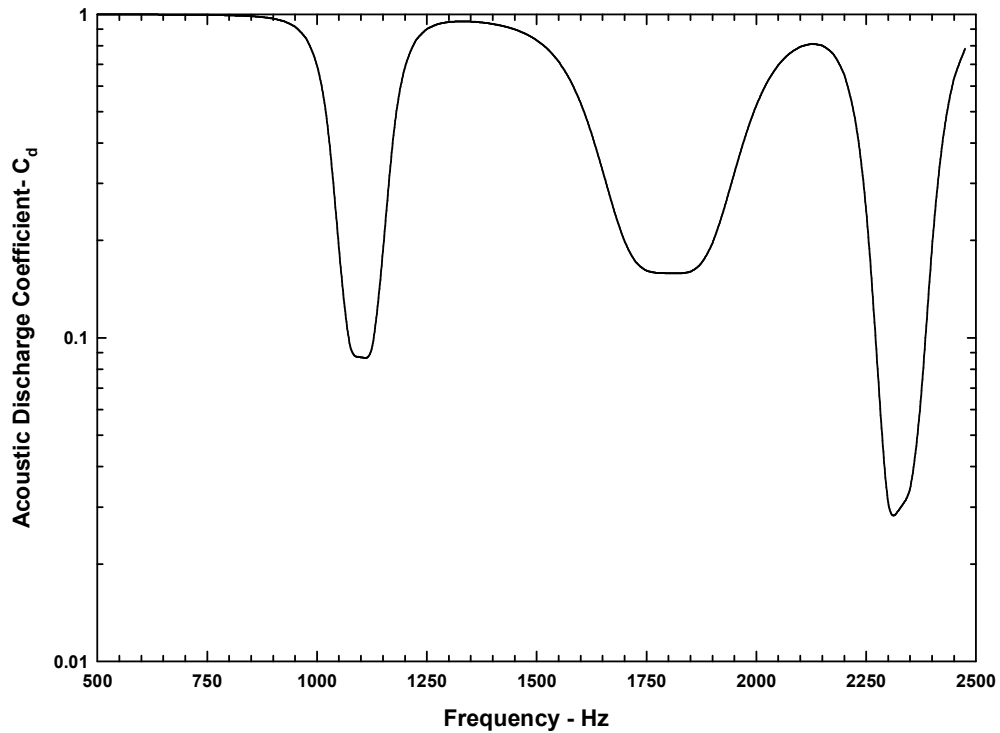

Figure 4.8c. 1-DOF Impedance Model Predicted Discharge Coefficient: SPL = 120 dB, Configuration S01L120; K = 1.1, H/Ws = 3.20
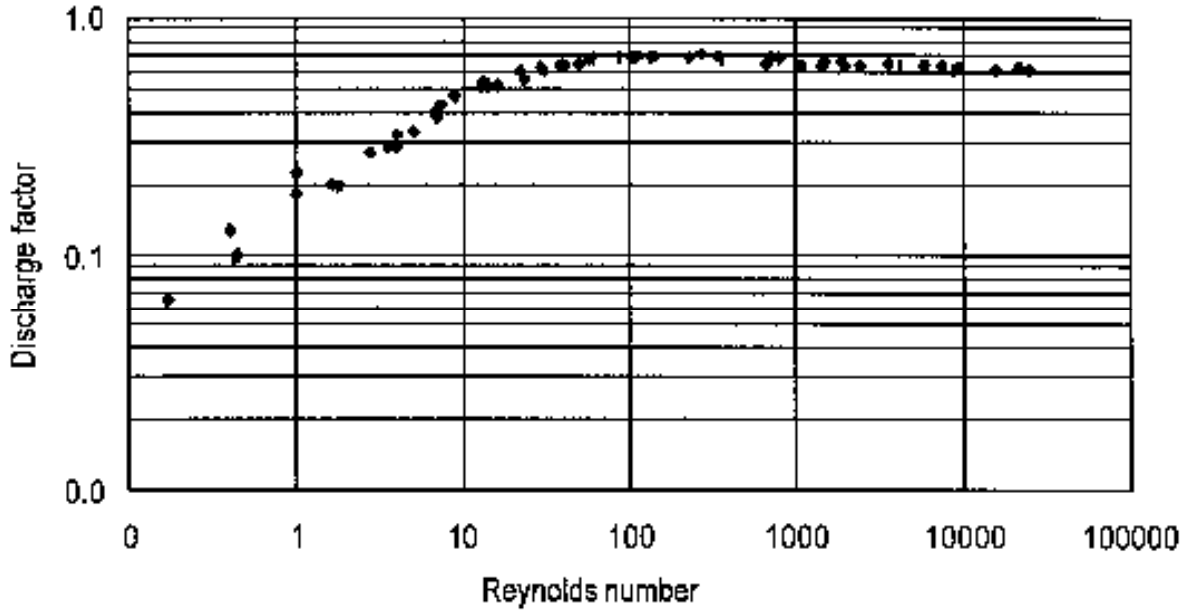
Figure 4.9. Steady-State Discharge Coefficient of Sharp-Edged Circular Orifices[6]

Derivation of a Non-Grazing Flow Radial (2-DOF) Control Volume Slit Liner Model.

The derivation of the 2-dof slit resonator impedance model is based on applying conservation of unsteady mass and vertical momentum across the control volume sketched in Figure 4.10. The quantities *"H"* and *"r_o"* denote the outer and inner surfaces of the control volume respectively. During the inflow half-cycle, the acoustic volume flow entering the control volume through the outer control surface is denoted by $u(H)\pi H$ and the acoustic volume flow entering the cavity through the inner control volume consists of an inviscid component, denoted by $u_{inv}W_{inv}$, and a boundary-layer component, denoted by $u_{BL}W_{BL}$.

The impedance model is derived for the half-cycle when the incident acoustic velocity is pumped into the resonator cavity - it is not valid during the other half-cycle when the acoustic velocity is ejected from the resonator cavity. The restriction of the model to the in-flow half-cycle is not unduly limiting because the particle volume flow pumped into and out-of the resonator volume must be constant over a dynamically steady-state sound period. Thus an approximate solution over the in-flow half-cycle should result in an approximate solution over the entire cycle. The derivation of the model assumes that all resonator dimensions are small compared to the wavelength of the incident sound field to distinguish Helmholtz resonators from quarter-wave tube resonators.

41
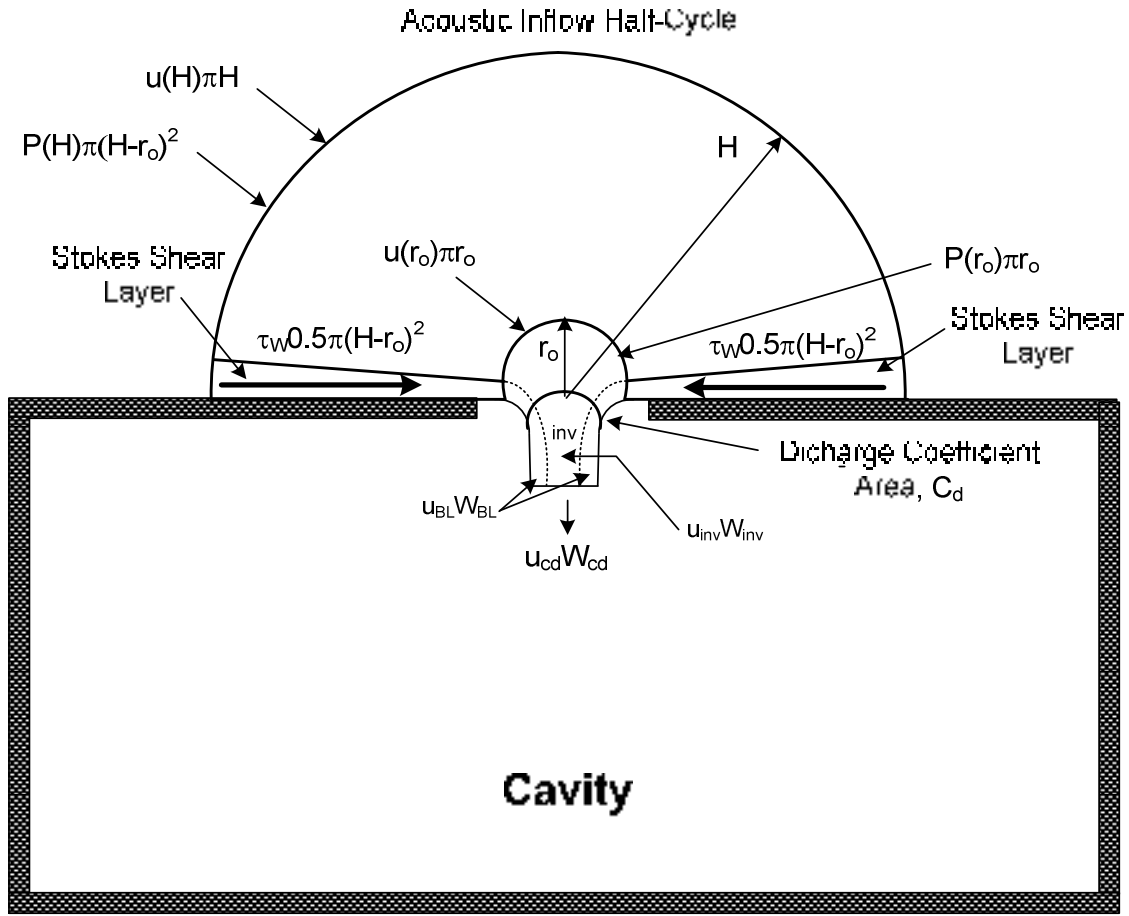
Figure 4.10. Control Volume used in 2-dof Slit Resonator Impedance Model Derivation

Conservation of Mass.   Assuming H << λ, Tempkin has shown that to lowest order, compressibility effects are small with respect to mass flow convection[1]. This approximation permits the conservation of mass flux into and out-or the control volume to be written, where the acoustic velocities are understood to be functions of time,

$$u_H \pi H = u_{cav} \pi r_o = u_{inv} W_{inv} + u_{BL} W_{BL} \qquad (4.1)$$

Thus the pumping of fluid into and out-of the slit orifice takes place in an unsteady, incompressible manner. Equation (4.1) shows that to first-order, the pumping of volume flow into and out-of a resonator orifice is governed by unsteady, incompressible motion. This makes sense because acoustic changes can occur only over scale lengths on the order of an acoustic wavelength.

Equation (4.1) contains the four unknown parameters u_{inv}, W_{inv}, u_{BL} and W_{BL}, which are very difficult to measure. The number of parameters will be reduced by adapting the discharge coefficient concept used to predict one-dimensional steady-state volume flow in ducts[3,4]. The

42

instantaneous inviscid volume flow, $u_{inv}W_{inv}$, and boundary layer volume flow, $u_{BL}W_{BL}$, are combined into a single volume flow, denoted as $u_{cd}W_{cd}$ in Figure 4.10. With this understanding, (1) is written

$$u_H \pi H = u_{cav}\pi r_o = u_{cd}W_{cd} \rightarrow \quad u_{cd} = \frac{u_{cav}}{\left(\dfrac{W_{cd}}{\pi r_o}\right)} = \frac{u_{cav}}{C_D} \tag{4.2}$$

Here $u_{cd}\,W_{cd}$ represents the instantaneous acoustic volume flow entering the cavity through a vena contracta area denoted as W_{cd} in Figure 1. Equation (4.2) introduces an acoustic discharge coefficient, C_d. Using experimental data to determine C_d is equivalent to determining the average volume flow rate entering/exiting the resonator cavity during each half-cycle[2,3].

Conservation of Radial Momentum. Referring to Figure 4.10, the conservation of momentum in the radial direction may be written,

$$\rho_o \pi \left(\frac{H^2 - r_o^2}{2}\right)\frac{du_{cav}}{dt} = \rho_o \left(u_H^2 \pi H - u_{cd}^2 C_d \pi r_o\right) + P_H \pi H - P_{cav}\pi r - \tau_w 2\left(H - r_o\right) \tag{4.3}$$

Using (4.2) to replace u_H by u_{cav} and u_{cd} by u_{cav}/C_d yields, after some modest algebra,

$$\rho_o \pi \left(\frac{H^2 - r_o^2}{2}\right)\frac{du_{cav}}{dt} = \rho_o \pi r_o \left(\frac{r_o}{H} - \frac{1}{C_d}\right)u_{cav}^2 + P_H \pi H - P_{cav}\pi r - \tau_w 2\left(H - r_o\right) \tag{4.4}$$

The various terms in (4.4) are described below.

- The term on the left-hand-side (LHS) represents the time rate of increase of momentum within the control volume. As shown schematically in Figure 4.10, H is a radial length parameter that is unknown and must be determined experimentally.

- The first term on the right-hand-side (RHS) represents the net radial momentum flux entering the control volume through its outer radial control surface.

- The sum of the second and third terms on the RHS represent the net radial acoustic driving force acting on the control volume. Here P_H represents the acoustic pressure driving the sound particle volume flow into the resonator cavity during the inflow half-cycle and P_{cav} represents the cavity restoring pressure.

- The fourth term on the RHS represents the momentum loss from frictional wall shear stresses τ_w distributed over the side wall housing the slit orifice.

Model Simplifications. The non-linearity of (4.4) prevents an analytic solution. It must be solved numerically to achieve a dynamically steady-state solution, followed by a Fourier transform to calculate the fundamental harmonic velocity component. Although this procedure is numerically straightforward, it greatly complicates the design of sound absorbing liners. Since our goal is to derive a reasonably accurate, but simple, impedance model, the following three simplifications are introduced to derive an approximate analytic solution.

Non-Linearity. The first simplification is based upon the hot-wire experiments of Ingard and Ising[2]. They showed, at high SPLs, the formation of alternating non-linear jetting into and out-of an orifice during each half-cycle. They also showed that the amplitudes of the higher harmonic velocity components were small relative to the fundamental. Physically, this permits the derivation of a model that ignores lower/higher harmonic energy and allows for harmonic oscillation of non-linear jetting into and out-of the orifice. With this understanding, the non-linear term u_{cav}^2 in (4.4) may be simplified to

$$u_{cav}^2 \cong \left| u_{cav} \right| u_{cav}(t) \cong u_{cav}^2 \, e^{i\omega t} \tag{4.5}$$

Substituting (4.5) into (4.4) yields,

$$i\omega\rho_o\pi\left(\frac{H^2 - r_o^2}{2}\right)u_{cav} = \rho_o\pi r_o\left(\frac{r_o}{H} - \frac{1}{C_d}\right)u_{cav}^2 + P_H\pi H - P_{cav}\pi r - \tau_w 2(H - r_o) \tag{4.6}$$

Here du_{cav}/dt was replaced with the expression, $i\omega u_{cav}$. The simplification achieved by ignoring higher harmonic energy permits the solution of (4.6) in the frequency domain rather than the time domain required in the solution of (4.4).

Cavity Pressure. The second simplification assumes that the cavity pressure can be accurately modeled by solving the one-dimensional wave equation in the cavity resulting in the following expression,

$$P_{cav} = -i\rho_o c_o \sigma \cot(kL_c) u_{cav} \tag{4.7}$$

Viscous Scrubbing Losses. The third simplification addresses the wall shear stress τ_w and assumes that it is generated by acoustically generated viscous scrubbing losses. A simple model based upon dimensional analysis is proposed. Acoustic shear stresses are derived assuming "Stokes-like" axially uniform diffusion of vorticity over the face-plate wall that is modeled as proportional to $\mu u_{cav}\sqrt{\omega/\nu}$. With these assumptions, the wall shear stress τ_w is written,

$$\tau_w \cong K_{vis}\mu_o u_{cav}\sqrt{\frac{\omega}{\nu_o}} \tag{4.8}$$

The parameter K_{vis} will be determined from NASA furnished impedance data.

Substituting (4.5), (4.7) and (4.8) into (4.6), dividing by πr_o, and rearranging yields,

$$\left(\frac{1}{C_d} - \frac{r_o}{H}\right)u_{cav}^2 + (r + ix)u_{cav} = \left(\frac{H}{r_o}\right)\left(\frac{P_H}{\rho_o}\right)$$

$$\text{where} \quad r = \frac{2}{\pi}\left(\frac{H}{r_o} - 1\right)K_{vis}\sqrt{\omega\nu_o}; \quad x = \frac{\omega r_o}{2}\left(\frac{H^2}{r_o^2} - 1\right) - c_o\sigma\cot(kL_{cav}) \tag{4.9}$$

The solution to (4.9) is

$$u_{cav} = \sqrt{\bar{C}_d\left(\frac{H}{r_o}\right)\left(\frac{P_H}{\rho_o}\right) - \left(\frac{\bar{C}_d}{2}\right)(r + ix)} - \left(\frac{\bar{C}_d}{2}\right)(r + ix)$$

$$\text{where} \quad \bar{C}_d = \frac{C_d\left(\frac{H}{r_o}\right)}{\left(\frac{H}{r_o} - C_d\right)} \tag{4.10}$$

With u_{cav} specified by (4.10), the slit resonator impedance is determined from the following expression,

$$Z = \frac{P_H}{\rho_o c_o \sigma u_{cav}} = \frac{P_H}{\rho_o c_o \sigma \left[\sqrt{\bar{C}_d \left(\frac{H}{r_o}\right)\left(\frac{P_H}{\rho_o}\right) - \left(\frac{\bar{C}_d}{2}\right)(r+ix)} - \left(\frac{\bar{C}_d}{2}\right)(r+ix) \right]}$$

$$= \sqrt{\left(\frac{1 - C_d \dfrac{r_o}{H}}{C_d}\right)\left(\frac{r_o}{H}\right)\left(\frac{P_H}{\rho_o c_o^2 \sigma^2}\right) + \left(\frac{r+ix}{2c_o\sigma}\right)^2} + \left(\frac{r+ix}{2c_o\sigma}\right) \tag{4.11}$$

The resonator resistance and reactance follow from (4.11) as shown below,

$$R = real(Z); \quad X = imag(Z) \tag{4.12}$$

<u>Model Validation</u>

The predicted impedance was compared to data furnished by NASA LaRC. The model parameter K_{vis} defined in (4.8) is used to force agreement between predicted and measured resistance. The parameters K_{vis}, C_d and H are coupled. They are used to force agreement between predicted and measured reactance. The interpretation of H is of interest. Figure 4.10 suggests that it is connected to the distance from the slit where the acoustic pressure is outside the near field of the slit. *In this sense, H may represent an initial step towards understanding how to effectively use the Dean Two-Microphone Impedance measurement method.*

In order to achieve reasonable agreement between prediction and data, the model was modified by decoupling the resistance and reactance. This was necessary because the high values of reactance were preventing any kind of reasonable agreement using (4.11) to predict resistance. Thus, (4.11) was modified as shown below,

$$R \cong \left(\frac{r}{2c_o\sigma}\right) + \sqrt{\left(\frac{1 - C_d \dfrac{r_o}{H}}{C_d}\right)\left(\frac{r_o}{H}\right)\left(\frac{P_H}{\rho_o c_o^2 \sigma^2}\right) + \left(\frac{r}{2c_o\sigma}\right)^2} \tag{4.13}$$

Figures 4.11a and 4.11b summarize the predicted vs. measured resistance and reactance of Configuration SO1 at SPL = 120 dB. As discussed above, the model parameters K_{ac} and H were selected to force agreement with data. As shown, reasonable agreement between prediction and data was achieved. The values of the discharge coefficient required to achieve even the modest agreement shown in Figures 4.11a and 4.11b are displayed in Figure 4.11c. They are disturbingly small. A possible explanation for this is suggested by the close agreement in impedance, displayed in Figure 4.12, for configurations S01L and S32L at SPL = 120 dB. This suggests that the acoustic behavior of the slit resonator cannot be modeled using a one-dimensional impedance model.
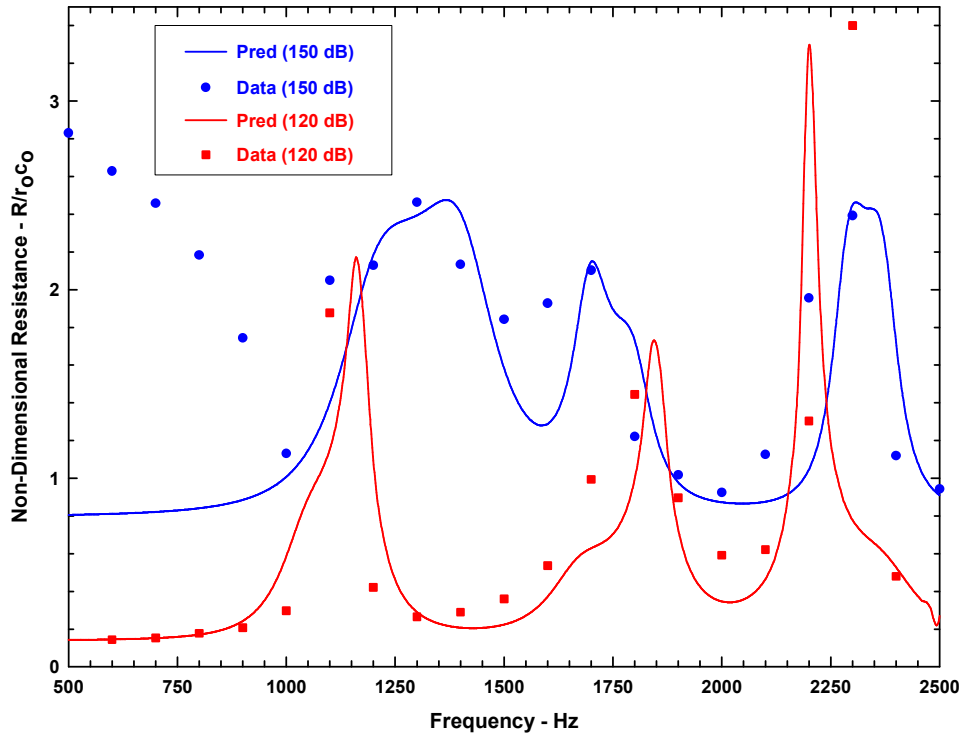
Figure 4.11. Predicted vs. Measured Slit S01L Resonator Resistance: SPL = 120/150 dB, $K_{ac}(120)$ = K(150) = 0.30, H(120) /W_S= 5.75, H(150) /W_S= 5.28
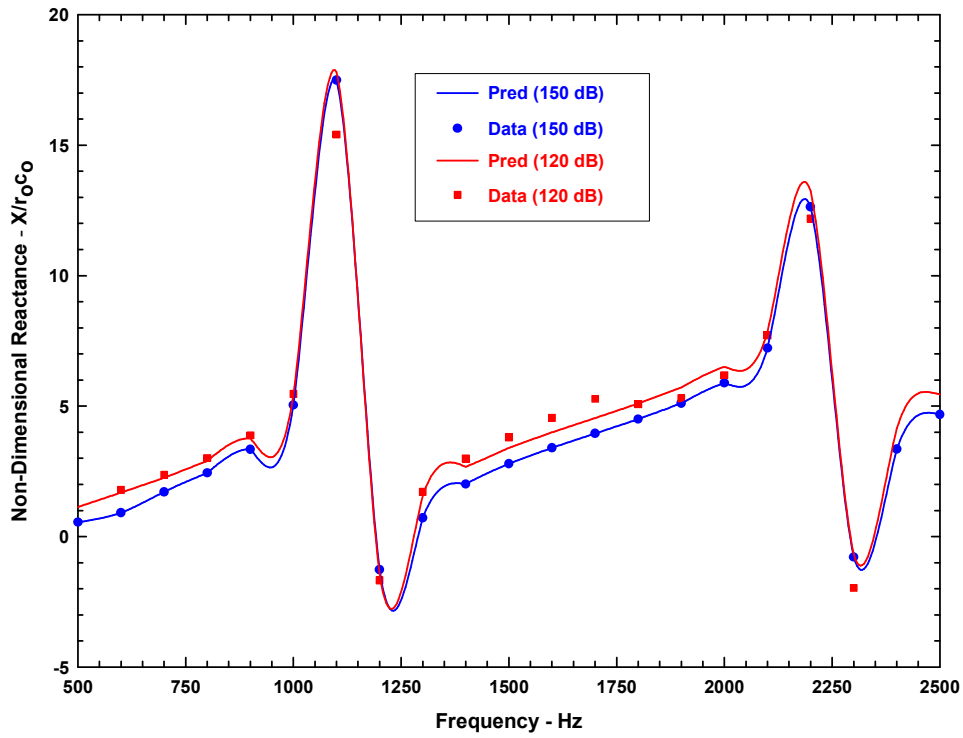

Figure 4.12. Predicted vs. Measured Slit S01L Resonator Reactance: SPL = 120/150 dB
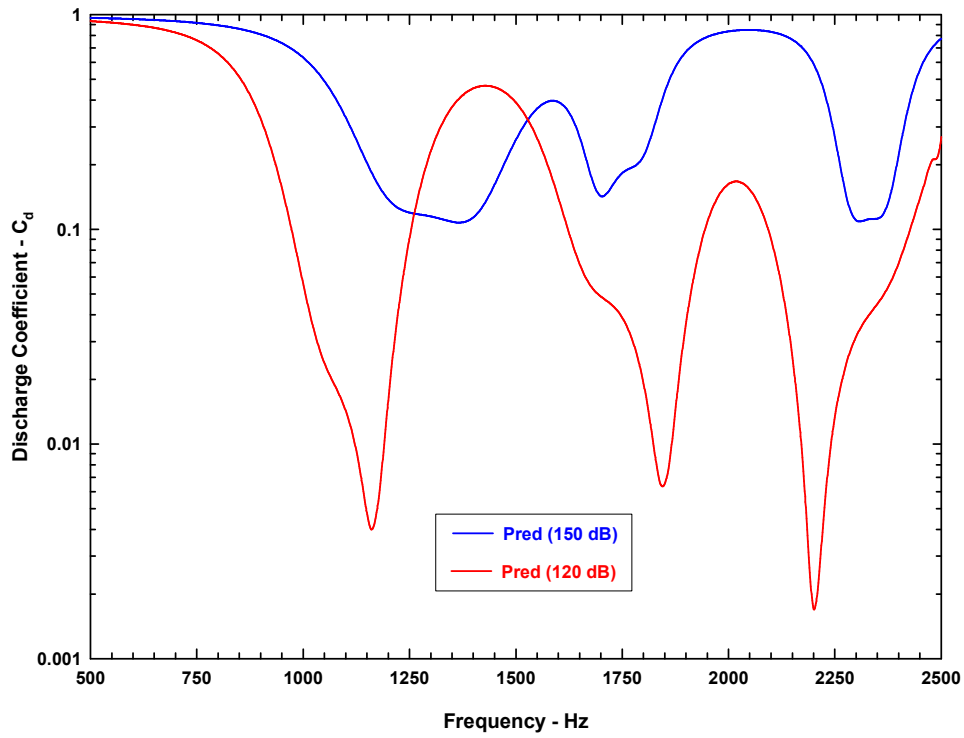
46

Figure 4.13. Slit Resonator Discharge Coefficient Required to Match Predicted S01L Resistance to Data: SPL = 120/150 dB
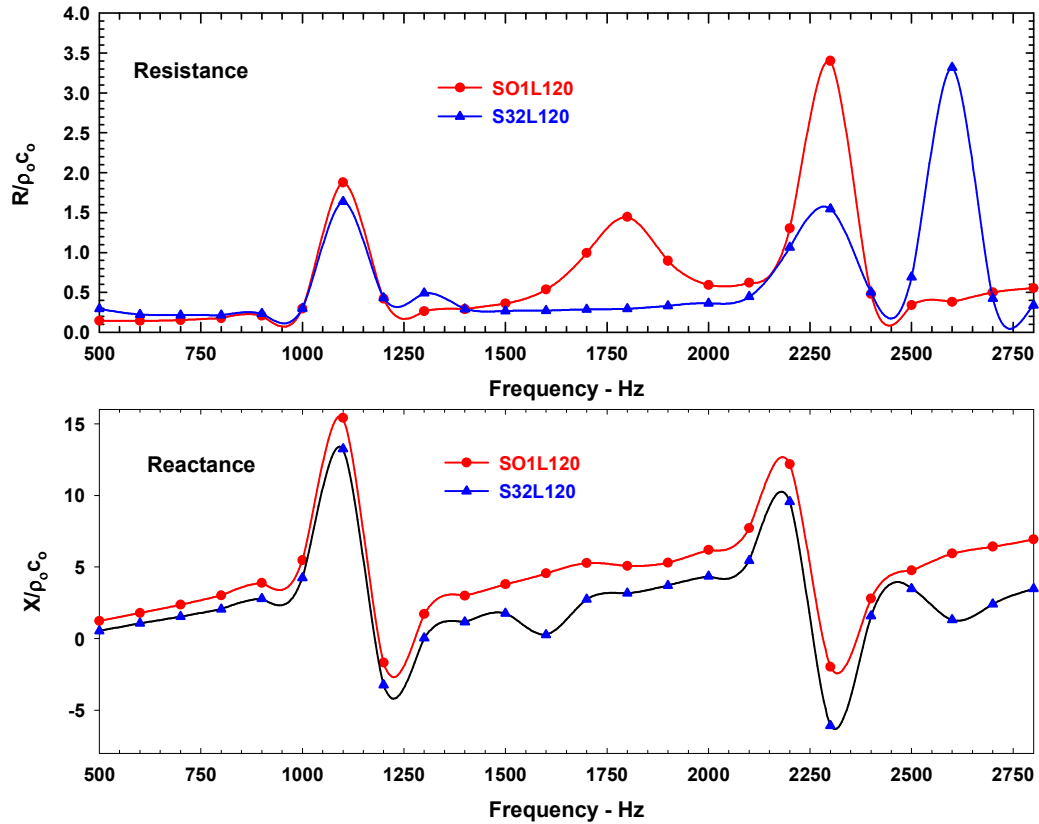

Figure 4.14. Impedance of Configurations S01L120 and S32L120

5. GRAZING FLOW IMPEDANCE MODEL of MULTI-CIRCULAR ORIFICES HELMHOLTZ RESONATORS

An axial (1-dof) control volume model was developed to predict the impedance of Helmholtz resonators constructed with multi-circular orifices exposed to intense sound and uniform grazing flow. Since the derivation of impedance model is quite similar to that derived in Sections 3 and 4, a detailed derivation is not presented.

Model Validation.

Figures 5.1 and 5.2 compare model predicted impedance with measurement for SPLs of 120 dB and 140 dB and grazing flow Mach numbers of 0 and 0.3 respectively. Observe that the second peak resistance displayed in the grazing flow data occurs at frequencies near resonance as shown in the flattening out of the reactance data above roughly 2000 Hz.

Although it is clear that a correlation exists between the resistance peaks and the local "flattening" out of the reactance, we do not understand the physical mechanism(s) causing this behavior.

The model empirical parameters need to be calibrated by a large database of impedance data.
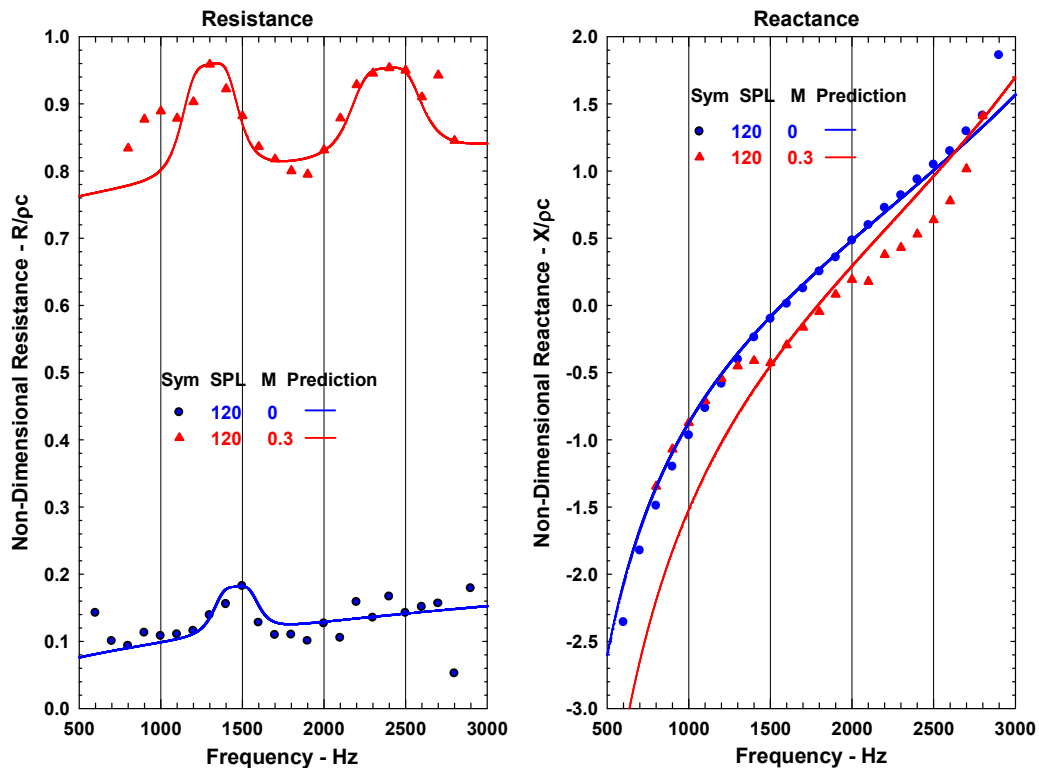

Figure 5.1. Measured/Predicted Effect of Mach No. on Impedance of Configuration GEATOL1, SPL = 120 dB, d_{ori} = 0.038-in, σ = 0.038, L_{cav} = 1.5-in, Hexagonal Cavity with 3/8-in face-to-face spacing

Figure 5.2. Measured/Predicted Effect of Mach No. on Impedance of Configuration GEATOL1, SPL = 140 dB, d_{ori} = 0.038-in, σ = 0.038, L_{cav} = 1.5-in, Hexagonal Cavity with 3/8-in face-to-face spacing
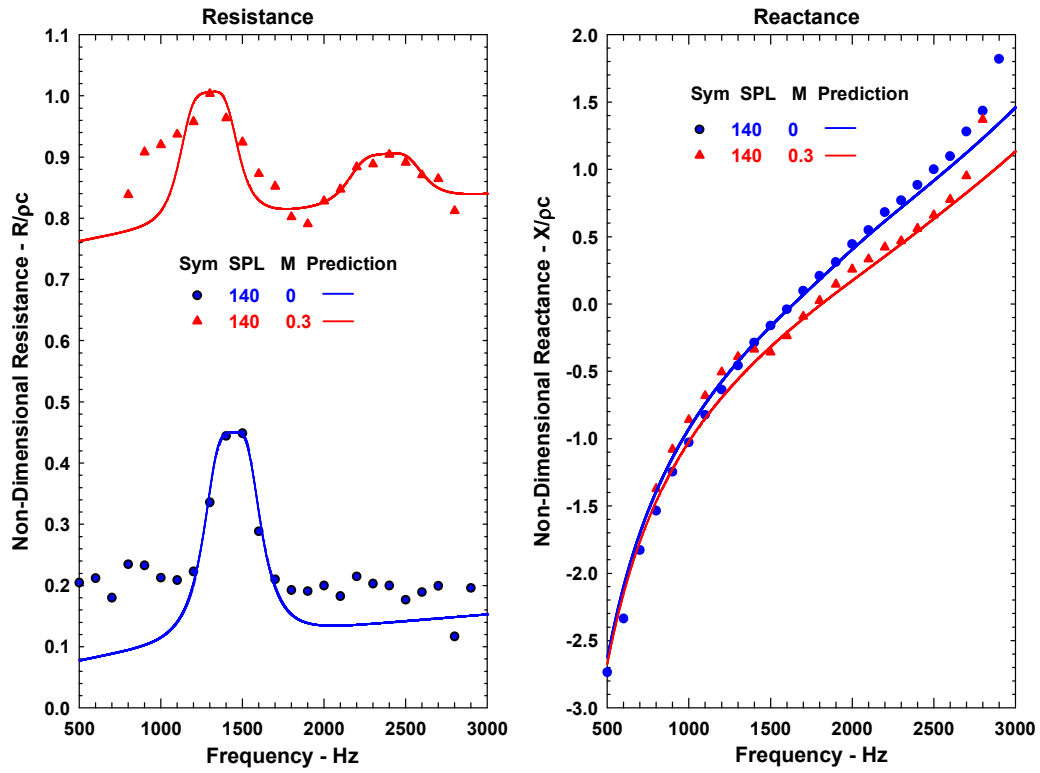
5. SUMMARY AND CONCLUSIONS

<u>Numerical Findings</u>

C. Summary and conclusions

In Phase I, computationally, we have made two significant advances in the application of computational aeroacoustics methodology to acoustic liner technology. We believe we are the first to investigate the effect of high temperature on liner performance by direct numerical simulation. High temperature liners are potential suppressor of turbine and combustion noise from jet engines. For resonators with the same depth mode resonance frequency, our finding indicates that temperature effects for discrete sound are not the same as for broadband noise. For discrete sound, the normalized resistance appears to be insensitive to temperature except at high SPL. However, reactance is lower, significantly lower in absolute value, at high temperature. Also, at high temperature, a liner generally has a larger absorption coefficient. For broadband sound, both the normalized resistance and reactance are not much affected by a large temperature increase for low frequencies. There are, however, noticeable differences in liner reactance at high frequencies. Absorption coefficient is nearly independent of temperature at low frequencies. But at higher frequencies, the absorption coefficient is higher at higher temperature.

Another technical advance we have made in Phase I work is to investigate computationally the acoustic performance of a liner. This, as far as we know, has not been done before. Previous works concentrate on a single resonator. A liner is an array of resonators. In an array of resonators, the resonators may interact acoustically. This interaction cannot be determined by studying a single resonator. Our preliminary work reveals that liner impedance is affected by the non-uniformity of the incident sound waves. That is, pressure gradient is important. This observation is new. It suggests mutual resonator interaction in the presence of a sound pressure gradient. The significance of this phenomenon is not fully understood. Further work is required to quantify the observed effect.

In regard to computer run time, for all single slit resonator computations reported above, the run time for discrete frequency incident sound using 4 cores on a 64-cores Microway computer cluster (AMD Opteron, 2GHz) is 11 hours. For computations involving 10 slit resonators, 40 cores are used with 4 cores per resonator. The run time is again about 11 hours. For 3 dimensional normal incidence impedance tube computations using 26 cores, the run time is about 4 days. It should be emphasized that because of the limited time available in Phase I, our computer codes have not been optimized. In addition, the code design is conservative; placing emphasis solely on computational accuracy. For instance, the codes are designed to be capable of computing accurately for frequencies up to 6 kHz. If the design criterion is reduced to 3 kHz, a significant reduction in the number of meshes becomes possible. As a result, we estimate that for 3D computation, there could be a factor of 3 reduction in computer run time.

<u>Impedance Modeling Findings</u>

The 1-dof and 1-dof resonator impedance model demonstrate the potential to predict fairly accurately resonator impedance as a function of SPL and grazing flow. It did so over only for a small database of resonator data. In order to extend the practical usefulness of these models, the empirical parameters used to predict impedance should be calibrated with a meaningful number of resonator impedance data.

The two-dimensional radial control volume impedance model offers the potential to empirically determine incident sound pressure face-plate distance from resonator orifices. This represents

an important initial step in improving our understanding of how to effectively use the Dean Two-Microphone impedance measurement method.

The local minimums/maximums of the slit/circular orifice impedance data may be generated by non-linear generated modulation of the orifice inflow/out-flow separation eddies. Modulation of the inflow/out-flow into the resonator cavity modulates the resonator resistance and reactance.

References

1. Temkin, S., *Elements of Acoustics*, John Wiley & Sons, 1981 pg. 177-190.

2. Schlichting, H., *Boundary-Layer Theory*, McGraw-Hill Book Company, pgs 176-178, 78-80,560, 1968.

3. Rosenhead, L. Editor, *Laminar Boundary Layers*, Oxford at the Clardendon Press, 439-446, 134-135,1963.

4. Ingard, U. and Ising, H., "Acoustic Non-Linearity of an Orifice", JASA, Vol. 42, No. 1. 6-17. 1967.

5. Hersh A. S, Walker, B. E. and Celano. J.E., "Helmholtz Resonator Impedance Model. Part 1. Non-Linear Behavior", Submitted to AIAA Journal, December 2001.

6. Johansen, F. C., "Flow Through Pipe Orifices at Low Reynolds Numbers", Proceeding of Royal Society, London, Vol. 26, Series A.